Article

Not peer-reviewed version

Computational Geometry Platform for Symmetry Breaking in Ellipsoids: Application to Shape Transitions and Curvature-Driven Self-Assembly Driving Force of Liquid and Soft Matter Drops and Capsules

David Uriel Zamora Cisneros , Matthew J. Harrington , Noémie-Manuelle Dorval Courchesne , Alejandro D. Rey *

Posted Date: 29 April 2026

doi: 10.20944/preprints202604.2051.v1

Keywords: biaxiality; triaxiality; spheroids; curvature; shape coefficient; umbilic points; lines of curvature

 doi:10.20944/preprints202604.2051.v1

Article

Computational Geometry Platform for Symmetry Breaking in Ellipsoids: Application to Shape Transitions and Curvature-Driven Self-Assembly Driving Force of Liquid and Soft Matter Drops and Capsules

David Uriel Zamora Cisneros [1], Matthew J. Harrington [2], Noémie-Manuelle Dorval Courchesne [1] and Alejandro D. Rey [1,*]

[1] Department of Chemical Engineering, McGill University, 3610 University Street, Montreal, QC, H3A0C5, Canada
[2] Department of Chemistry, McGill University, 801 Sherbrooke Street West, Montreal, QC, H3A0B8, Canada
* Correspondence: alejandro.rey@mcgill.ca

Abstract

This paper develops, implements, and uses integrated global and local geometric modelling of ellipsoids and transforms curvatures and shapes into energy metrics that predict potential curvature-driven self-assembly driving force pathways into fibers and films. Global parameterization is based on eccentricities and the local parameterization, based on mean and Gaussian curvatures, is mapped into shape and curvedness parameterizations that clearly distinguish critical shape effects from curvedness effects in contrast to mean and Gaussian curvatures. Finally, the geometric modelling is transformed, through a liquid membranology model, into bending energy densities that point the ways to fiber and film assembly pathways.

Keywords: biaxiality; triaxiality; spheroids; curvature; shape coefficient; umbilic points; lines of curvature

1. Introduction

Invariably, shape, size, and structure (known as $\mathfrak{S}^3$ metrics), play a dominant role in material processing and functionalities of synthetic and biological material systems [1–6]. Industrial application examples include shapes and sizes of storage tanks, aerofoil wings, turbine blades, and so on [7–11]. Biological materials have incorporated precise control of size, structures, and shapes as in bird feathers, flower petals, plywood and more [12–16]. In anisotropic soft matter, as in protein-based precursors, as in protein-based precursors, there are several examples in which organisms including mussels, spiders, velvet worms, and hagfishes, utilize fluid condensates including colloidal liquid crystals and coacervates to fabricate complex hierarchically structure materials following stimuli response and self-assembly mechanisms [17–21] of precisely controlled size, shape, and liquid crystalline structural order [18,19,22–27]. However, the most studied liquid crystal droplets and shells happen to be near-spherical conditions, which conveniency provides valuable but incomplete insight into a baseline for studying and classifying a broader variety of shapes, sizes, structures, textures, and even defects.

The symmetry breaking of spheres into biaxial and triaxial convex shapes then, can be used as a fertile ground for the understanding and characterization of $\mathfrak{S}^3-$dependent material science and engineering phenomena. Ellipsoids exhibit a shape spectrum with promising tuning capabilities of form- and curvedness-dependent effects on material processing (such as self-assembly, self-organization, viscosity, etc.) [28–33], and material functionality (friction, wetting, adhesion, load-bearing, etc.) [34–37]. This rich variety of shapes and structural properties is observed in several in-vivo [19,38–40], in-vitro [19,27,41–43], and in-silico [27,38,41,44–46] systems in fields such as physics, biology, and

 doi:10.20944/preprints202604.2051.v1

engineering. Figure 2 shows the symmetry breaking of a spherical shape into the ellipsoidal spectrum where structures deviate from the sphere to the cylinder and rod-like shapes with the emergence of critical curvature points known as umbilic dots (red dots) whose characterization is crucially important as in tetravalency [47–49] of drops and particles [50–55] and umbilic-surface vortex interaction in fluid mechanics [56–58].

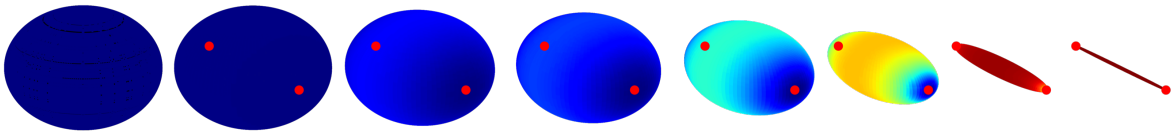

Figure 1. Schematic of a sphere morphing into a cylinder, and passing through a shape spectrum of biaxial prolate ellipsoids. The heatmap scheme represents relative shape coefficient (S) values on the surface as the minor axes linearly decrease to a minimum. Shades of blue represent sphere-like shape coefficients $S \approx -1.0$, and shades of red represent cylinder-like shapes $S \approx -0.5$. The red markers at both ends denote umbilic points at which principal curvatures are equal (see Section 2 for discussion of dimensionless normalized shape coefficient S).

There are several representative examples of ellipsoids in nuclear physics, biology, soft matter, architecture, and astronomy. In physics, ellipsoids appear in the classical approach to understanding atomic and nuclear models [54,59]. The nuclear model considers the nucleus as an incompressible fluid with a surface energy that is minimized when its structure approximates sphericity. This is the case for nuclei with small atomic mass, where the surface energy dominates over the Coulomb repulsion, maintaining a spheric shape [54,59]. However, in certain cases, small-enough deformations ensuring a constant volume (isochoric) may allow deviation from this shape while keeping stability with shapes like prolate/oblate ellipsoid [59]. The surface energy which competes with the repulsion forces, in the simpler of nuclear models (not involving quantum effects) like the drop model, is constructed using a surface-tension pressure approach which directly relates the surface energy with the mean curvature [54,60,61]. These shapes are also reflected in more recent nuclear physics models where an ellipsoidal atomic nucleus is modeled to illustrate energy levels and decay pathways [59,62,63], serving as a bridge between microstructures and microscopic properties.

In biology and engineering, from a purely material perspective, ellipsoids play a role through multiple scales (see Figure 3 from cellular to architectural scales). Examples include cells, membranes and shells where ellipsoidal shapes are needed for optimized confinement designs, offering robust mechanical stability, sound storage principles, and pathways for self-assembly, self-organization, and even curvature-driven motility [6,27,50–52,64–67]. For instance, red blood cells, which can be approximated to a type of oblate ellipsoids, optimize surface area while maintaining integrity and reducing aggregation under shear flow [6,67–69], excluding the transport advantages that come with it, as opposed to prolate-like morphologies that tend to align under shear flow while allowing for shape modification under osmotic or other driving forces [40,70,71].

 doi:10.20944/preprints202604.2051.v1

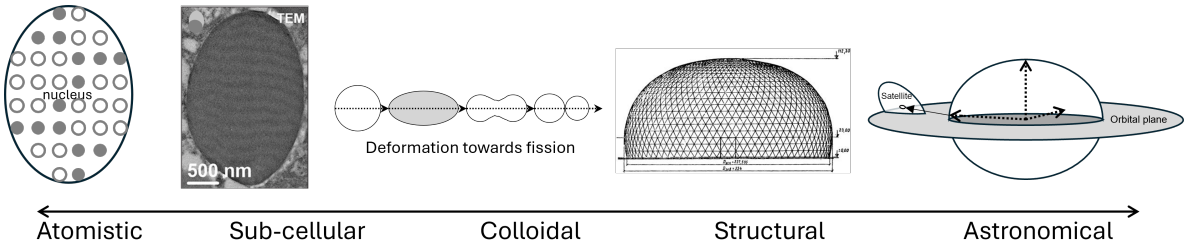

Figure 2. Schematic of multiscale ellipsoidal shapes throughout different fields and length scales. From left to right: (1) atomistic model of certain nuclei with ellipsoidal shape, highlighting the protons(neutrons) in filled(unfilled) gray marker without orbitals distinction [54,72]. (2) Schematized drop model exemplifying deformation toward droplet fission, applied to colloidal particles and atom models [54,55]. (3) Tactoidal mussel byssus core vesicle containing smectic liquid crystal collagenous molecules [70]. (4) architectural ellipsoidal-dome design for their load bearing and aesthetic features in [8]. (5) astronomical body with their orbit shape from [73] Panels adapted from [54,55,73]. Panel from [70] reprinted in part with permission from (2026) American Chemical Society. Panel from [8] used with permission of American Society of Mechanical Engineers (2026); permission conveyed through Copyright Clearance Center, Inc.

Liquid crystal vesicles provide an example where the interplay between storage principles and the symmetry breaking transition is connected to the processing of multifunctional and high-performance materials [74,75]. Of particular interest are the liquid crystalline protein precursors that form the mussel byssus [71], in which the accurate and efficient description of the shapes and sizes of liquid crystalline biological collagen-based polymer vesicles is a key challenge [46,70,76]. Recent microfluidic experiments [77] show the undergoing alignment of a lamellar liquid-crystalline structure and the prolate-like ellipsoidal mussel byssus core vesicles using shear flow for fiber formation, however the integration and coupling between the hydrodynamics, the liquid-crystalline alignment and the macrostructure is yet to be completely understood. Some other investigations focus on the coupling of ellipsoidal structures to orientational order, hence allowing for a pattern formation that minimizes free energy promoting different phenomena (mass transfer, mechanical stability, shape transitions, vesicle morphogenesis) under given constraints [78–82].

Engineering, architecture, and optics, take a wider range in the perspective of ellipsoidal forms as an inspiration to understand foundational principles for functional purposes [41,83]. A good example is the optimization of load distribution for high stability and storage, for acoustics [84,85], and light redirection [8,31,41]. Broader in scope, ellipsoidal shapes have also been used to model astronomical phenomena from the more accurate oblate ellipsoidal form of the Earth, to cosmic trajectories, wave propagation and other phenomena on celestial scale (e.g., liquid crystalline materials on stars' mantle) [61,73]. This predominance of quadric surfaces is schematized in Figure 3.

Ellipsoids, despite their ubiquity, as stated by Farouki [86], have seemingly simple definition, like other types of special symmetric curved surfaces (e.g., quadrics, surfaces of revolution). However, in practice, they pose a challenge in their numerical description and an integrated framework for a generic global-local characterization of ellipsoidal structures using curvedness/shape-based principles remains incomplete.

Classical approaches to ellipsoidal shapes often rely on parameterizations with standard measures such as mean curvature (H), the Gaussian curvature (K), and deviatoric curvature (D); which commingle shape and curvedness, and hence provide restricted insights into relevant geometrical features such as umbilics, points on surfaces where both principal curvatures are identical $\kappa_1 = \kappa_2$, where the deviatoric curvature is zero $(D = 0)$, and where the surface locally behaves as a sphere. This particular phenomenon encapsulates a plethora of geometrical features that could be exploited for tuning local and global features that govern material, mechanical, and energetic stability. Differential geometry offers a powerful language for dealing with these gaps by describing the curvature invariants that contain decoupled shape and curvedness information. It also admits the use of a coordinate-independent description with the Monge parameterization.

 doi:10.20944/preprints202604.2051.v1

Valuable descriptors for complex surfaces, in addition to the important $\mathfrak{S}^3-$metric, are enabled by establishing a curvedness/shape (C, S) methodology [46,74,76,87,88]: the Casorati curvature for quantitatively quantifying curvedness and the shape coefficient for quantitatively characterizing the anisotropy and symmetry-breaking of local surface patches. This novel (C, S) approach in soft matter geometry extricates and separates shape and curvedness (C) by introducing a dimensionless normalized shape coefficient (S): $-1 \leq \tan(\pi S/2) = H/D \leq +1$. In previous work, we have established and validated the (C, S) methodology [46,76]. Here we extend the application of this geometry-based toolbox to the ubiquitous ellipsoidal shapes, present across different phenomena and spatial scales (see Figure 3). To bridge the multiscale phenomena, we also include a global approach which captures classic shape and size modelling of ellipsoids [62]. We use the eccentricities (e_1, e_2) and look at the Monge patch surfaces for constant-volume and constant-shape evolution.

As mentioned above, in this work a robust computational toolbox is presented to compute key curvature metrics on parametric ellipsoidal surfaces, including umbilics and lines of curvature (LOC) near them. This curvature information is extracted and analyzed using a thermodynamic-geometric perspective to connect it to physical phenomena [46]. The specific objectives of this work are as follows:

1. Present and apply an efficient global shape characterization of biaxial and triaxial ellipsoids based on dual eccentricities.
2. Compute global ellipsoidal shape phase diagrams and identify pathways for spheroidization, fibrillization, and discoidization.
3. Develop and apply a local ellipsoidal shape characterization based on classical mean (H) and Gaussian (K) curvatures.
4. Introduce a local mapping from the commingled shape (H, K) characterization into the unmixed shape-curvedness (C, S) framework.
5. Provide an exhaustive characterization of the local shape metrics of ellipsoids, including generation, location, charge, and types of umbilic critical points.
6. Introduce the liquid crystal membranology methodology to endow the local description of ellipsoids with bending energy E_B.
7. Use the shape-energy connection to predict self-assembly driving force pathways for fiber and film formation for capsules containing liquids and soft matter materials.

This paper is organized as follows:

- Section 2 begins with a brief review on differential geometry and its application to an ellipsoidal parameterization in Section 2.2, thoroughly derived in Appendix A. The governing equations, constraints/intervals, and curvature concepts are developed in Sections 2.1-2.3 and listed in Tables 1 and 2 where main curvature concepts are delineated. The nondimensionalization of parameterized surfaces was carried out for visualization purposes, yielding dimensionless curvatures and volumes, as stated in Section 2.1.1 and shown in Figure 4. Section 2.4 introduces a direct connection between our methodology and classic curvature-based and elasticity models. Finally, Section 2.5 describes the computational methods used for the results in the following section.
- Section 3 discusses the results for three key generic ellipsoidal cases listed in Table 1. The curvature and shape coefficients of each case are included in Sections 3.1-3.2 including their curvedness/shape mappings.
- Section 4 establishes relevant study cases where the curvedness/shape methodology poses a valuable role in the description of membranology phenomena introduced in Section 2.4 and introduces possible and important curvature-based self-assembly driving force pathways for soft matter and liquid drops and capsules.
- Section 5 concludes the paper by outlining key results, novelty, significance, contributions to soft matter ellipsoids, and future work.
- Finally, Appendix C lists supplementary information on curvature energy and LOC for all relevant cases.

 doi:10.20944/preprints202604.2051.v1

Table 1. Three ellipsoidal cases used throughout this paper in their global parameterization.

Generic Forms	General Biaxial Prolate	General Biaxial Oblate	General Triaxial Ellipsoid
Intervals	$e_1 = e_2 \in (0,1]$	$e_1 = 0, e_2 \in (0,1]$	$e_2 = \sqrt{2}e_1 \in (0,1]$
Constant Volume case $\bar{V}$	$e_1 = e_2 \approx 0.5$	$e_1 = 0, e_2 \approx 0.64$	$e_1 \approx 0.4, e_2 = \sqrt{2}e_1$

Table 2. Summary of the curvature concepts and their relations with each other, the definition with the principal curvatures and its values at umbilics. Adapted from [87].

Curvature	Relations	Principal Curvatures	Umbilics
Mean, H	$\sqrt{C^2 - D^2}$	$(\kappa_1 + \kappa_2)/2$	κ_i
Gaussian, K	$H^2 - D^2$	$\kappa_1\kappa_2$	κ_i^2
Casorati, C	$\sqrt{H^2 + D^2}$	$\sqrt{(\kappa_1 + \kappa_2)/2}$	κ_i
Deviatoric, D	$\sqrt{H^2 - K}$	$(\kappa_1 - \kappa_2)/2$	0

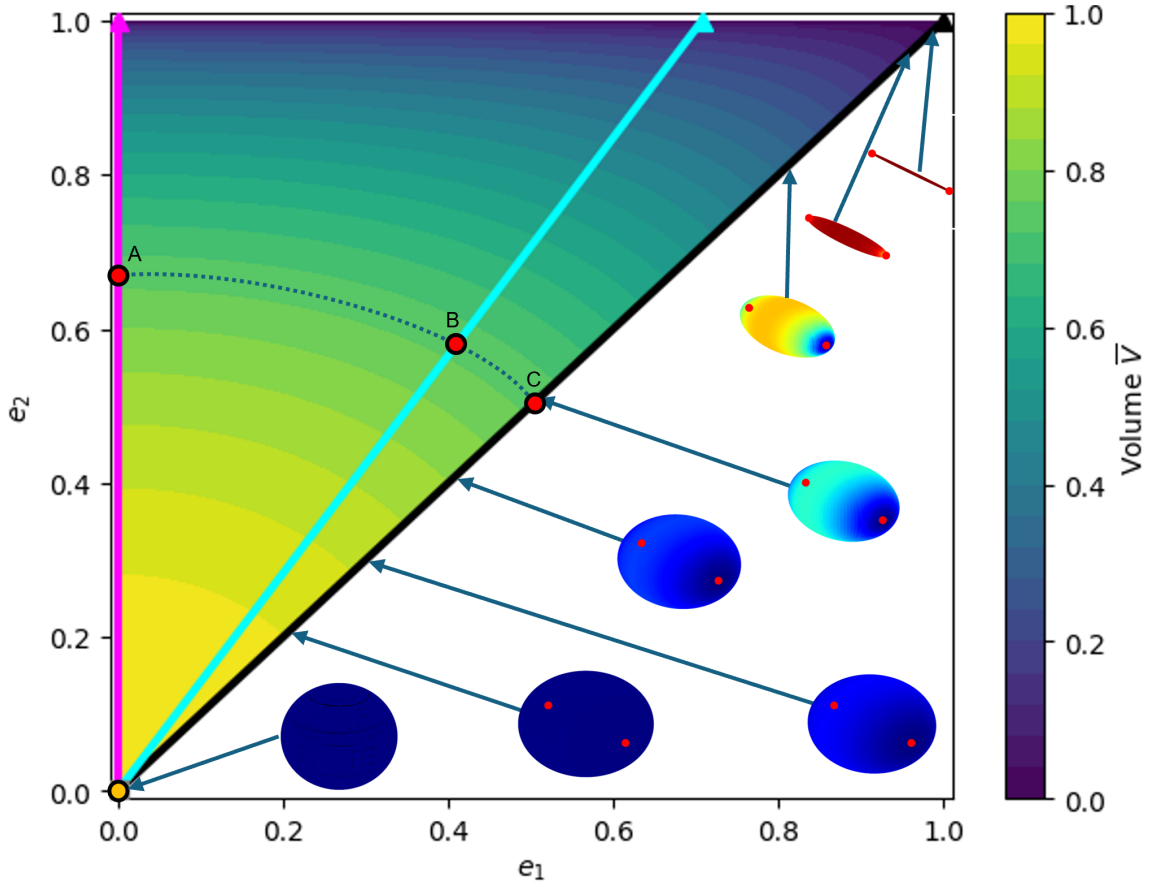

Figure 3. Eccentricity (e_1, e_2) shape-space with its level-set curves according to the definitions in the global parameterization in Section 2.1.1 for different dimensionless volumes $\bar{V}$. The three lines represent the three ellipsoidal classes analyzed listed in Table 1: oblate (magenta), generic triaxial (cyan), and prolate (black). Includes the linear shape spectrum in Figure 2 with the same color-coded shape coefficient values S. The dashed arc-line shows an isochoric pathway that represents the three ellipsoidal classes: (A) oblate biaxial; (B) triaxial; and (C) prolate biaxial ellipsoids, listed in Table 1 and further discussed in Sections 3.1-3.2.

 doi:10.20944/preprints202604.2051.v1

In partial summary, the results of the paper elucidate the emergence of critical umbilic points and potential self-assembly driving forces when traversing the fundamental curvedness/shape ellipsoidal space under various degrees of global anisotropy, global shape, and volume.

2. Materials and Methods

In this section, we present the methods and governing equations used throughout the paper, which expands on the connections between geometry and topology on spherical and non-spherical ellipsoids. To reach self-containment, we have included sufficient and necessary details on differential geometry, key curvature concepts, and definitions, and governing equations (see Appendices A-C for supplementary information and extended derivations). First, we introduce the global characterization of ellipsoids, and the three general cases analyzed in this work. Appendix A includes derivations and supplementary information.

2.1. Global Parameterization

2.1.1. Constraints and Restrictions

Without loss of generality, in rectangular (x, y, z) coordinates, let the semi-axes of an ellipsoid be a major axis, and (b, c) intermediate and minor axes respectively, so that they follow:

$$\frac{x^2}{a^2} + \frac{y^2}{b^2} + \frac{z^2}{c^2} = 1, \qquad a \geq b \geq c \tag{1}$$

Then, we introduce the eccentricities (e_1, e_2) which characterize all three ellipsoidal axes in the form:

$$e_1 = \sqrt{1 - \frac{b^2}{a^2}}, \quad e_2 = \sqrt{1 - \frac{c^2}{a^2}} \tag{2}$$

so that the two minor axes are a function of both eccentricities

$$b = a\sqrt{1 - e_1^2}, \qquad c = a\sqrt{1 - e_2^2} \tag{3}$$

which is possible if $a > 0$. In this form, the volume can be described using the eccentricities

$$V = \frac{4}{3}\pi a^3 \sqrt{1 - e_1^2}\sqrt{1 - e_2^2} \tag{4}$$

However, the relationship in Eq 1 requires that this volume follows

$$e_2 = \sqrt{(\bar{V}^2 + e_1^2 - 1)/e_1^2} \tag{5}$$

$$0 \leq e_1 \leq e_2 \leq 1 \tag{6}$$

For $a = 1$, equations 5-6 dictate that a maximum volume is obtained when $e_1 = e_2 = 0$, where the volumes approach that of a unit sphere $V_{us} = \frac{4}{3}\pi$. Then, a degenerate ellipsoid corresponds to the upper limit when $e_1 \to 1, e_2 \to 1$ and volume tends to $V \to 0$. In future computations, we use this definition of volume (V_{us}) for the nondimensionalization of the ellipsoidal volumes $\bar{V}$ computed in this work, as show in Figure 4. We note that the case of variable a is not explored in this paper, but Eq 4 shows that for a constant volume V^*, the corresponding surface is:

$$a = \left(\frac{3V^*}{4\pi}\right)^{2/3} \left(\frac{1}{(1 - e_1^2)^{1/6}(1 - e_2^2)^{1/6}}\right) \tag{7}$$

and the parameterization is 3D (a, e_1, e_2).

Therefore, in our 2D (e_1, e_2) parameterization, the two general cases can of biaxial ellipsoids of revolution are: the prolate $(e_1 = e_2)$ and the oblate ellipsoid $(e_1 = 0, e_2 > e_1)$. We consider a third

 doi:10.20944/preprints202604.2051.v1

case, the general triaxial ellipsoid, by introducing the arithmetic mean square sum between two axes, referred to as a general triaxial ellipsoid. In this way, a maximum volume for the triaxial case is set to $1/\sqrt{2}$ as shown in Figure 4, a condition seen in morphological and curvature studies of vesicles constriction [89]. Following the interval in Eq 1 so that:

$$b^2 = \frac{a^2 + c^2}{2} \tag{8}$$

$$e_2 = \sqrt{2} e_1 \tag{9}$$

In this way, the generic features of the global characterization are defined, including the three representative general cases used in this work, and listed in Table 1.

2.2. Local Parameterization

Curves and surfaces can be studied in differential geometry using established differentiable equations under certain constraints [90]. In this work, the local parameterization involves describing the surface with a Monge patch. This is an efficient way to describe a parametric surface $\mathbf{M}(u,v) = \mathbf{M}(x(u,v), y(u,v), z(u,v))$ [47], here represented as a $uv-$space of an open set in $\mathbb{R}^2$ [91]. Conceptually, in this work the Monge patch $\mathbf{p}(p_1, p_2)$ mainly represents fundamental extrinsic, and intrinsic concepts in surface geometry theory generally defined with parameters (p_1, p_2). These curvature concepts are connected to the first $\mathbf{g}$ and second fundamental forms $\mathbf{B}$, key properties of differential geometry [92].

The parametric relationship is mapped to a Monge patch using a vector-valued $\mathbf{s}(p_1, p_2) = [s_1(s_1, p_2), s_2(p_1, p_2), s_3(p_1, p_2)]^T$ which can be applied to the key parameters in the global parameterization (e_1, e_2) for a fixed a. Let us define a generic vector-valued $\mathbf{s}(u,v)$ which maps the uv-space into the three-dimensional space:

$$\mathbf{s}(u,v) = [e_1(u,v), e_2(u,v), \mathbf{M}(u,v)]^T \tag{10}$$

where $\mathbf{M}$ represents any of the ellipsoidal parameterizations presented in Appendix A. Then, surface metric tensor is described in the first fundamental form, and its coefficients (E, F, G) [47,93], as:

$$\mathbf{g} = \begin{bmatrix} 1 + \left(\frac{\partial \mathbf{s}}{\partial u}\right)^2 & \left(\frac{\partial \mathbf{s}}{\partial u}\frac{\partial \mathbf{s}}{\partial v}\right) \\ \left(\frac{\partial \mathbf{s}}{\partial u}\frac{\partial \mathbf{s}}{\partial v}\right) & 1 + \left(\frac{\partial \mathbf{s}}{\partial v}\right)^2 \end{bmatrix} = \begin{bmatrix} E & F \\ F & G \end{bmatrix} \tag{11}$$

with the induced arc-length $\mathrm{d}\mathbf{s}$:

$$\mathrm{d}\mathbf{s}^2 = \mathbf{g} : \mathrm{d}x\, \mathrm{d}x \tag{12}$$

with a determinant $\det \mathbf{g} > 1$, thus, the metric tensor is invertible so that:

$$\mathbf{g}^{-1} = \frac{1}{\det \mathbf{g}} \begin{bmatrix} G & -F \\ -F & E \end{bmatrix} \tag{13}$$

Using the notation from Eq 11 and Eq A39, the second fundamental form $\mathbf{B}$, known as the symmetric curvature $\mathbf{B}$ tensor, is:

$$\mathbf{B} = \begin{bmatrix} L & M \\ M & N \end{bmatrix} \cdot \frac{1}{\det \mathbf{g}} \begin{bmatrix} G & -F \\ -F & E \end{bmatrix} = \frac{1}{EG - F^2} \begin{bmatrix} LG - MF & -LF + ME \\ MG - NF & -MF + NE \end{bmatrix} \tag{14}$$

The first and second fundamental form, and the classical curvature concepts, can be defined in 2×2 tensor bases using an identity tensor $\mathbf{I}$. A traceless surface deviatoric tensor $\mathbf{q}$ defines the mean (H) and deviatoric (D) curvatures considering no off-diagonal terms. Contributions from a tensor alternator yield $\mathbf{B} = H\mathbf{I} + D\mathbf{q}$ where a given value for D characterizes the non-sphericity

 doi:10.20944/preprints202604.2051.v1

(sphere: $D = 0$) [87]. Then, from the Eq 14 mixed form, the classical curvature concepts, the mean (H), and Gaussian (K) curvature are:

$$H = \frac{1}{2}\mathrm{tr}(\mathbf{B}) = \frac{LG - 2MF + NE}{2(EG - F^2)} \tag{15}$$

$$K = \det(\mathbf{B}) = \frac{NL - M^2}{EG - F^2} \tag{16}$$

The deviatoric (D), Casorati (C), and shape coefficient (S), used for the description of the curvedness and shape are:

$$K = -C^2 \cos(2\pi) \tag{17}$$

$$H = C \sin\left(\frac{S\pi}{2}\right) \tag{18}$$

$$D = C \cos\left(\frac{S\pi}{2}\right)\sqrt{H^2 - K} \tag{19}$$

$$C = \sqrt{2H^2 - K} \tag{20}$$

$$S = \frac{2}{\pi}\arctan\frac{H}{\sqrt{H^2 - K}} \tag{21}$$

Generalized fundamental shapes are characterized with the shape coefficient $S = \{0, \pm 1/2, \pm 1\}$. Primary shapes are assigned to saddle $(S = 0)$, cylinders $(S \pm 1/2)$, and spherical cup $(S \pm 1)$, where the $\pm$ sign defines directionality according to the definition of the normal to the tangent space [48]. In this work we follow the convention concave-up (negative), concave-down (positive). The shapes follow a continuous spectrum defined by normalized parameter interval (e.g., Figure 2). The Casorati curvature, however, quantifies how curved a surface is [87,88], which varies within $C = [0, +\infty)$, where a planar surface with no curvature is $C = 0$. Also, the deviatoric curvature is non-negative: $D \geq 0$.

As mentioned above, this paper formulates, develops, and solves a variety of differential geometry-material science models using high-performance computing techniques coupled to shape-based spaces that uncoupled the distinct contributions of curvedness and shape. The formulation (see objectives in Section 1) has a two-step mapping form:

$$\underbrace{\mathbf{s}(e_1, e_2)}_{\text{Local Parameterization}} \xrightarrow{\text{global-to-local map}} \underbrace{(H, D) \rightarrow \mathbf{s}(e_1, e_2)}_{\text{Coupled Curvedness/Shape}} \xrightarrow{\text{local-to-global map}} \underbrace{(C, S) \rightarrow (H, D)}_{\text{Unmixed Curvedness/Shape}}$$

In the first mapping, the global parameterization of spheres, biaxial and triaxial ellipsoids is mapped into local curvatures (H,D), and the second local-to-local mapping results in a curvedness-shape space with spheres ($0D$, point), biaxial ellipsoids ($1D$, lines), and triaxial ellipsoids ($2D$, areas) according to the values of the ellipsoidal axes (a, b, c) and their eccentricities (e_1, e_2). As mentioned above, the (C, S) decouples shape and curvedness and directly identifies critical points such as umbilics $(S = +/-1)$, and sheds light on location of high curvedness, both of importance to soft matter self-assembly, as discussed in Section 1, Section 2.3 Section 2.4. Integration of structure into the $\mathfrak{S}^3-$model, such as smectic A LC drops [70,71] is left to future work.

2.3. Lines of Curvature and Umbilic Points

Shapes have been characterized using LOC, delineating the orthonormal principal curvature vector $\kappa_i = (\kappa_1, \kappa_2)$ along the surfaces. Certain regions in these surfaces exhibit particular cases where the principal curvatures are the same. These are the umbilical points or umbilics. Umbilical points possess essential information of the surface geometry which have recently started to be explored with passive and active systems, including curvature-controlled phenomena. For passive systems, they are relevant in the study of defect formation, disclinations, self-assembly and colloidal interaction [52,94].

 doi:10.20944/preprints202604.2051.v1

On the other hand, some works have identify a potential use for growing tissue, mechanics in active nematics, and ordering-dependent processes like budding of closed surfaces, like in membranes [50–52] or like the deformation and fission in the droplet model [53–55].

It is known that the principal curvatures κ_1, κ_2 are $\mathrm{eig}(\mathbf{B})$, thus from Eq 14:

$$\det(\mathbf{B} - \kappa_i \mathbf{I}) = 0 \tag{22}$$

$$\kappa_{1,2} = H \pm \sqrt{H^2 - K} = H \pm D \tag{23}$$

which clearly define these points as global minima of the right-hand side (the full derivation is included in Appendix C); as noted above D is non-negative.

We have followed the conversion of the surface and set it in a Monge patch form. With the principal curvatures κ_i defined in Eq 23, it is known that the umbilics are precisely located at the $H^2 - K = 0$ point where the deviatoric curvature D is zero and has a global minimum so that we have the surface gradient [48] is

$$D = 0, \qquad \nabla D = 0 \tag{24}$$

and the LOC behave in a particular way around these points [90] (see Table 2 and Appendix C). The network patterns are generally classified in lemon, monstar and star, according to the Darbouxian definition [48,90,95] and an umbilic charge defined by a curvature line index. Fundamental studies in differential geometry fully describe and clearly define a total index of $+2$ for our spheroidal shapes [47–49,95–98]. This is depicted in the case for the oblate and prolate cases where two non-generic umbilics with charge $+1$ are in located at the poles; and four umbilics enclosed by a lemon-like LOC network on a triaxial ellipsoid possess a $+1/2$ charge. In terms of the eccentricities, the umbilics are located at:

$$x = \pm a \sqrt{\frac{e_1^2}{e_2^2}}, \qquad y = 0, \qquad z = \pm a \sqrt{1 - e_2^2} \sqrt{\frac{e_1^2}{e_2^2}} \tag{25}$$

Hence, they follow the charge conservation, as expected for the symmetry breaking of the biaxial cases into the triaxial ellipsoid [48]. We have identified the lemon-like pattern for the generic triaxial ellipsoid (see Figure A4). Appendix C shows the LOC network for the three special cases considered in Table 1. Table 2 summarizes the key and computable curvature concepts.

2.4. Liquid Crystal Membranology for Ellipsoids

In this section we present and apply the liquid crystal membranology (LCM) method [99–101] that endows the geometric ellipsoids with local bending and torsion elastic energies:

$$\underbrace{\text{Geometric Ellipsoids}}_{\text{global}(e_1,e_2),\text{local}(H,K),\text{local}(C,S)} \xrightarrow{\text{LCM}} \underbrace{\text{Local Energy of Ellipsoids}}_{\text{Bending and Torsion Elasticity}}$$

Thus, we enlarge the $\mathfrak{S}^3$ description to include local curvature elasticity by attaching an infinitesimally thin membrane endowed with bending and torsion modes; by endowing the ellipsoid's surface with elasticity we assume that there is no effect on shape itself. These generalized metrics provide additional information on self-assembly driving forces and self-organization of actual ellipsoids, such as LC tactoids [6,22,24,50–52,64,67,70].

The geometric framework $(H, K)|(H, D)$ appears naturally in the elasticity theories, models, textures, and characterization of nematic, smectic, cholesteric and other LCs [99–104]. In addition, elasticity models for interfaces, membranes [105–109] can also be cast into $(H, K)|(H, D)$ frameworks using methods that identify the geometric orientation $\mathbf{k}$ with the material average orientation unit vector $\mathbf{n} : k = \mathbf{n}$, characterizing the LCM method. Likewise, the elasticity of filaments, rods, ropes, and

 doi:10.20944/preprints202604.2051.v1

fibers can be described by the line LC model which identifies the fiber unit tangent $\mathbf{t}$ with the material director $\mathbf{n}$. The objective of this subsection is to focus on a relevant representative examples: $2D$ LC biological membranes that are relevant to our ellipsoid's geometry and their critical umbilical points, the formulation process is as follows:

i First, we apply the classical LCM to obtain the well-known Helfrich elastic free energy model and to establish the connection between membrane bending and torsion and the classical splay and saddle-splay deformations, thus connecting membrane moduli with the elastic moduli of LCs.
ii Secondly, we reformulate the LCM model in the uncoupled (C, S) framework.
iii Thirdly, we use (i-ii) to establish connections between local Helfrich elasticity and umbilics.

(i) Liquid Crystal Membranology. The connection between LC and biological membranes was pioneered by Helfrich who developed the approach denoted by nemato-membranology, which, as mentioned above, is based on identifying the orientational director $\mathbf{n}$ with the membrane unit normal $\mathbf{k}$ [106,110–112]. For example, the elasticity of biological lipid bi-layer membranes is accurately described by the well-known Helfrich energy E_H for bending $2k_cH^2$ and saddle-splay $\bar{k}_cK$ [113,114], which opposed to the Euler-Lagrange Equation, does not consider the tension tensor contributions, following the linear bending-like approach [115] or for tensionless membranes [116]:

$$E_{HT} = 2k_cH^2 + \bar{k}_cK + \gamma \tag{26}$$

where γ is the surface tension, $H = \mathbf{I}_s : \mathbf{B}/2$ is the average curvature, $K = \det(\mathbf{B}) = H^2 - D^2$ the Gaussian curvature, $\mathbf{B} = -\nabla_s\mathbf{k}$ is the symmetric curvature tensor, $\nabla_s(.) = \mathbf{I}_s \cdot \nabla(.)$ is the surface gradient operator, $\mathbf{I}_s = \mathbf{I} - \mathbf{kk}$ is the surface unit tensor, and D is the deviatoric curvature. Since in the present context γ is considered to be always a constant, we then define the bending-torsion free energy density E_H:

$$E_H = E_{HT} - \gamma = 2k_cH^2 + \bar{k}_cK \tag{27}$$

Eq 26 follows the nematic Frank elastic energy E_F [113,117]:

$$\begin{aligned} E_F = \frac{K_1}{2}(\nabla \cdot \mathbf{n})^2 + \frac{K_2}{2}(\mathbf{n} \cdot \nabla \times \mathbf{n})^2 + \frac{K_3}{2}(\mathbf{n} \times (\nabla \times \mathbf{n}))^2 \\ - \frac{K_{24}}{2}\nabla \cdot (\mathbf{n}\nabla \cdot \mathbf{n} + \mathbf{n} \times (\nabla \times \mathbf{n})) \end{aligned} \tag{28}$$

where K_1 is the splay, K_2 is the twist, K_3 is the bend, and K_{24} is the saddle-splay constants.

Replacing the director $\mathbf{n}$ with the outer unit normal $\mathbf{n} \equiv \mathbf{k}$ in Eq 26, and considering tangential deformation gradient ∇_s using $\nabla \times \mathbf{k} = 0$ [100,118] yields:

$$E_F = (\frac{K_1}{2} + 4K_{24})H^2 + (-2K_{24})K \tag{29}$$

which coincides with the Helfrich free energy model E_H, and gives the bending and torsion moduli in terms of Frank constants: $4k_c = (K_1 + 8K_{24}), \bar{k}_c = -2K_{24}$. The zero curl $\nabla \times \mathbf{k} = 0$ follows directly the condition of parallel layering [100,105,118] (see Appendix B).

 doi:10.20944/preprints202604.2051.v1

(ii) Liquid Crystal Membranology in the Local Formulation. Now we reformulate the Helfrich model in Eq 26 into our local (C, S) framework using the uncoupled local mapping (see Section 2.2, Eqs 15-18) resulting in:

$$\begin{aligned} E_H(C,S) &= (2k_c + \bar{k}_c)C^2 \sin^2\left(\frac{S\pi}{2}\right) - \bar{k}_c C^2 \cos^2\left(\frac{S\pi}{2}\right) \\ &= \left[(2k_c + \bar{k}_c)\sin^2\left(\frac{S\pi}{2}\right) - \bar{k}_c \cos^2\left(\frac{S\pi}{2}\right)\right] C^2 \end{aligned} \tag{30}$$

$$E_H(C,S) = \underbrace{\left[(\frac{K_1}{2} + 2K_{24})\sin^2\left(\frac{S\pi}{2}\right) - \bar{k}_c \cos^2\left(\frac{S\pi}{2}\right)\right]}_{\text{shape energy}} \underbrace{C^2}_{\text{curvedness energy}} \tag{31}$$

Table 3 shows the Helfrich membrane energy (Eq 31) of primitive shapes: sphere, saddle, and cylinder. These results are comparable to systems where the bending energy is dominating, like in a monodispersed globules with imposed incompressibility conditions using monodispersed spheres of a given radius to ultimately characterize microemulsion shapes [109]. The ratio between the membrane energies of these primitive shapes can be reduced to a ratio between the between k_c and $\bar{k}_c$.

Table 3. Helfrich energy E_H in Eq 31 for three primitive shapes (n.b. the sign for the sphere and cylinder cases depend on the definition of the unit normal direction).

Primitive Shape	**Shape Coefficient** S	**Membrane Energy** $E_H(C,S)$
Sphere	$S = \pm 1$	$E_{H,\text{sph}} = (2k_c + \bar{k}_c)C^2$
Saddle	$S = 0$	$E_{H,\text{sdl}} = k_c C^2$
Cylinder	$S = \pm 1/2$	$E_{H,\text{cyl}} = -\bar{k}_c C^2$

The connection between primitive shape energies then is that of a mean average:

$$\begin{aligned} E_H(C, \pm 1/2) &= \frac{E_H(C,\pm 1) - E_H(C,0)}{2} \\ &\rightarrow \text{cylinder energy} = \frac{\text{dome energy} + \text{saddle energy}}{2} \end{aligned} \tag{32}$$

In cases of interest where focusing on pure curvature-driven phenomena, the geometric Helfrich E_H in Eq 31 is defined as a dimensionless bending elasticity $\bar{E}_B$:

$$E_H = 2k_c H^2 + \bar{k}_c H^2 - \bar{k}_c D^2 \tag{33}$$

$$\bar{E}_B = \frac{E_H}{2k_c + \bar{k}_c} = H^2 - \frac{\bar{k}_c}{2k_c + \bar{k}_c} D^2 = H^2 - \left(1 - \frac{2}{2 + \bar{k}_c/k_c}\right) D^2 \tag{34}$$

As mentioned above, by considering $4k_c = (K_1 + 8K_{24},\ \bar{k}_c = -2K_{24})$ we find:

$$\bar{E}_B = \frac{E_H}{\frac{K_1}{2} + 2K_{24}} = H^2 + \left(\frac{2K_{24}}{\frac{K_1}{2} + 2K_{24}}\right) D^2 \tag{35}$$

If typical values [119] of the ratio $\bar{k}_c/k_c$ are $-1 < \frac{\bar{k}_c}{k_c} < -0.8$, then:

$$\bar{E}_B = H^2 - \left(1 - \frac{2}{1.1}\right) D^2 = H^2 + 0.81 D^2 = C^2 - 0.19 D^2 \tag{36}$$

The equation of bending elasticity $\bar{E}_B$ indicates that for a fixed C, bending decreases with increasing S through the square sign function and that for a fixed shape $\bar{E}_B$ increases quadratically with C.

 doi:10.20944/preprints202604.2051.v1

For a given biaxial prolate ellipsoid, we find higher energy in the polar region than in the equatorial region, while for the biaxial oblate ellipsoid the reverse is true. In section 4.1 and Figure 5 we present and analyze $\bar{E}_B$ based on these observations.

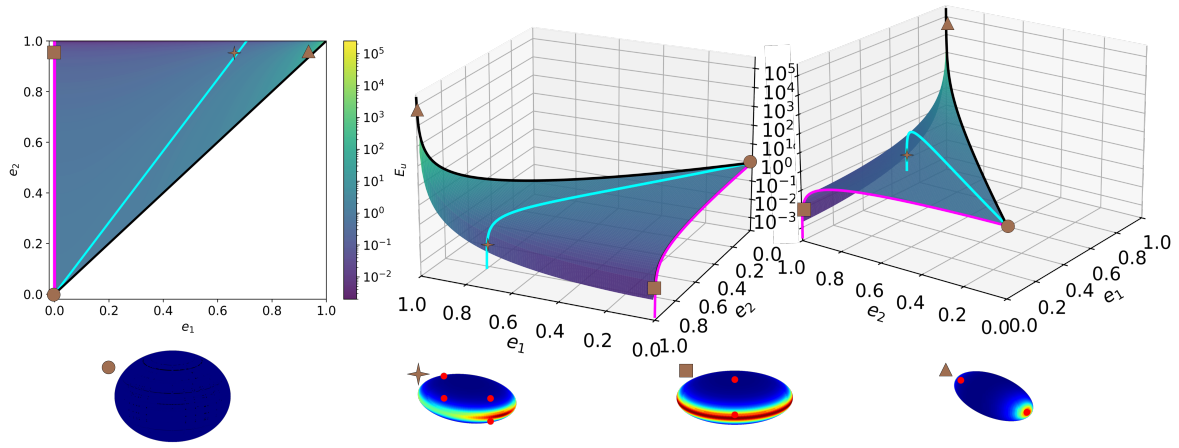

Figure 4. Umbilic curvature energy E_u landscape as a function of (e_1, e_2) eccentricities. Top row: $2D$ top view (left); $3D$ view (middle) of the bending energy E_B evaluated at the umbilics; and a clockwise 90-degree rotated image (right) from the same landscape. The three lines represent the three general cases in Table 1: oblate (magenta), generic triaxial (cyan), and prolate (black). Lower row: The markers on the landscape show limiting cases, representing the final processes defined as: Spheroidization at $e_1 \approx 0.95, e_2 = e_1/\sqrt{2}$ (star); Discoidization at $e_1 = 0, e_2 \approx 0.95$ (square); Fibrillization at $e_1 = e_2 \approx 0.95$ (triangle) of a sphere (circle) $e_1 = e_2 = 0$; and the $2D$ Ellipsoidization $0 < e_1 < 0$, $e_2 = 1$ region. The visual representation of each ellipsoid is included using color-coded shape coefficient S to include the close shape/curvedness mapping. The E_u axes are in log-scale.

(iii) Curvo-elasticity of Umbilics. As mentioned above (Section 2.3), umbilic points are defined when $D = 0, S = \pm 1$ and $K = H^2$. Using $\bar{E}_B$, the umbilic energy E_u is defined by:

$$E_u = \bar{E}_B(D = 0, S = \pm 1) = H^2 = K = C^2 \tag{37}$$

The critical nature of the umbilics is then reflected in the equality of the three curvatures.

The charge of the two(four) biaxial(triaxial) ellipsoid umbilics is $+1(+1/2)$.

Section 3.1 shows the $\bar{E}_B$ energy of $+1$ umbilics in the biaxial prolate ellipsoid limit of fibers, and biaxial oblate ellipsoid limit of disks are:

$$+1 \text{ umbilics on fibers} : E_{u,f} = \lim_{e_1 = e_2 \to 1} E_u \to \infty \tag{38}$$

$$+1 \text{ umbilics on disks} : E_{u,d} = \lim_{e_1 = 0, e_2 \to 1} E_u \to 0 \tag{39}$$

The case of the $+1/2$ umbilics in generalized triaxial ellipsoids' surfaces is discussed in Section 3.2, Figure 6.

 doi:10.20944/preprints202604.2051.v1

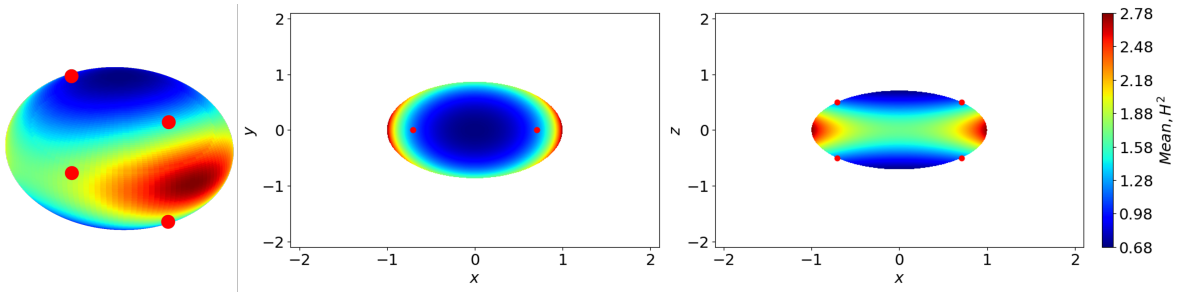

(**a**)

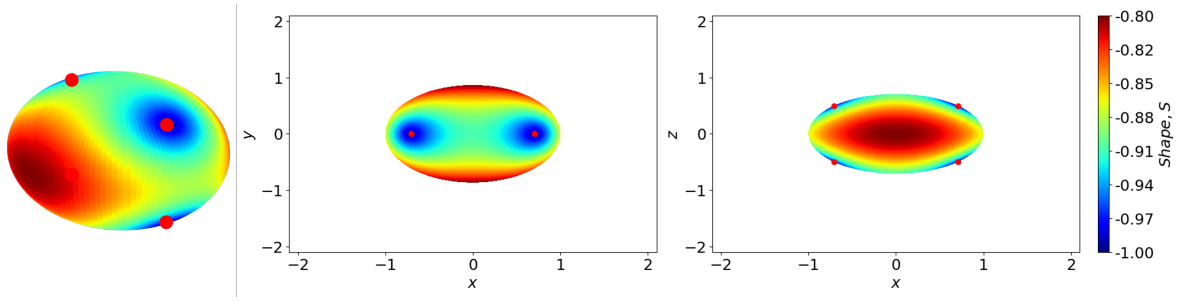

(**b**)

Figure 5. $3D$, top and side views of an general triaxial case $e_1 \approx 0.4, = e_2 = \sqrt{2}e_2$ with heatmaps of curvature conceptualizations: mean curvature H and shape coefficient S. The four umbilical points with $+1/2$ charge are located with a red marker. (**a**) The squared mean curvature H^2 scale is color-coded. (**b**) The shape coefficient S scale is color-coded.

2.5. Computational Methods

The computational sequence follows well-established methodology for the calculation of the first and second fundamental form, and differential geometry literature [47,93]. The numerical computation of the principal curvatures follows the robust algorithm introduced in previous works [86,90] and recently applied to geometric and thermodynamic studies [46,87]. The principal curvatures which comprised the LOC are computed by solving a set of equations defined by the coefficients of the first $(\mathbf{g})$ and second fundamental $(\mathbf{B})$ forms shown in Section 2.2 to produce an orthonormal network at Eq 10. Then, the $\mathbf{s}(u, v)$ describe the changes in the semi-axis a, b, c with respect to the arc-length r, following the principal direction of tangent vectors (see Appendix A). Thus, a given principal curvature κ is computed with:

$$\frac{\mathrm{d}e_1}{\mathrm{d}r} = \eta(M - \kappa F) \quad \text{and} \quad \frac{\mathrm{d}e_2}{\mathrm{d}r} = -\eta(L - \kappa E) \tag{40}$$

or

$$\frac{\mathrm{d}e_1}{\mathrm{d}r} = \mu(N - \kappa G) \quad \text{and} \quad \frac{\mathrm{d}e_2}{\mathrm{d}r} = -\mu(M - \kappa F) \tag{41}$$

where (E, F, G), and (L, M, N) are the coefficients of the first and second fundamental forms (see Section 2.2), and (η, μ) are non-zero coefficients defined by:

$$\begin{aligned} \eta &= 1/\sqrt{\left(E(M - \kappa F)^2 - 2F(M - \kappa F)(L - \kappa E) + G(L - \kappa E)^2\right)} \\ \mu &= 1/\sqrt{\left(E(N - \kappa G)^2 - 2F(M - \kappa F)(N - \kappa G) + G(M - \kappa F)^2\right)} \end{aligned} \tag{42}$$

 doi:10.20944/preprints202604.2051.v1

and arc-length

$$\mathrm{d}r = \sqrt{E(\mathrm{d}e_1)^2 + 2F\mathrm{d}e_1\mathrm{d}e_2 + G(\mathrm{d}e_2)^2} \tag{43}$$

The orthogonal LOC network is computed by solving the ODEs system in Equations 40-43 at a point every point in Eq 10 considering the following criterion. The sign of the direction following every step at a given point on the surface is purely defined by local geometry and contained in the maximum and minimum principal curvatures (κ_1, κ_2) [86,87], stated in Eq 23. Since the model is arc-length parameterized, the computation of the arc-length is carried out for every step. Hence, a balance between the geometric space and a sufficiently small step-size is required for good resolution, solution stability and computational time. It is also recommended to split the system according to the respective axial symmetry for further optimizing calculations.

Figure 7 summarizes the generic aspects of the computational methodology in going from ellipsoidal geometry (input) to self-assembly driving force pathways (output) using the following sequence that reflects the objectives of the paper (Section 1):

1. Find the principal curvatures.
2. Calculate the classic H, K, D curvatures that commingle curvedness and shape.
3. Map the local H, D curvatures into our unmixed curvedness and shape metrics (C, S).
4. (a) Characterize all ellipsoids in the $(C, S)-$space. (b) Characterize the nature, number, location, and energy of umbilics.
5. Determine the umbilics energy and local bending energy E_B on any point of the ellipsoids by using a liquid crystal membranology approach.
6. Identify potential self-assembly driving force pathways for rods (fibrillization) and films (discoidization).

 doi:10.20944/preprints202604.2051.v1

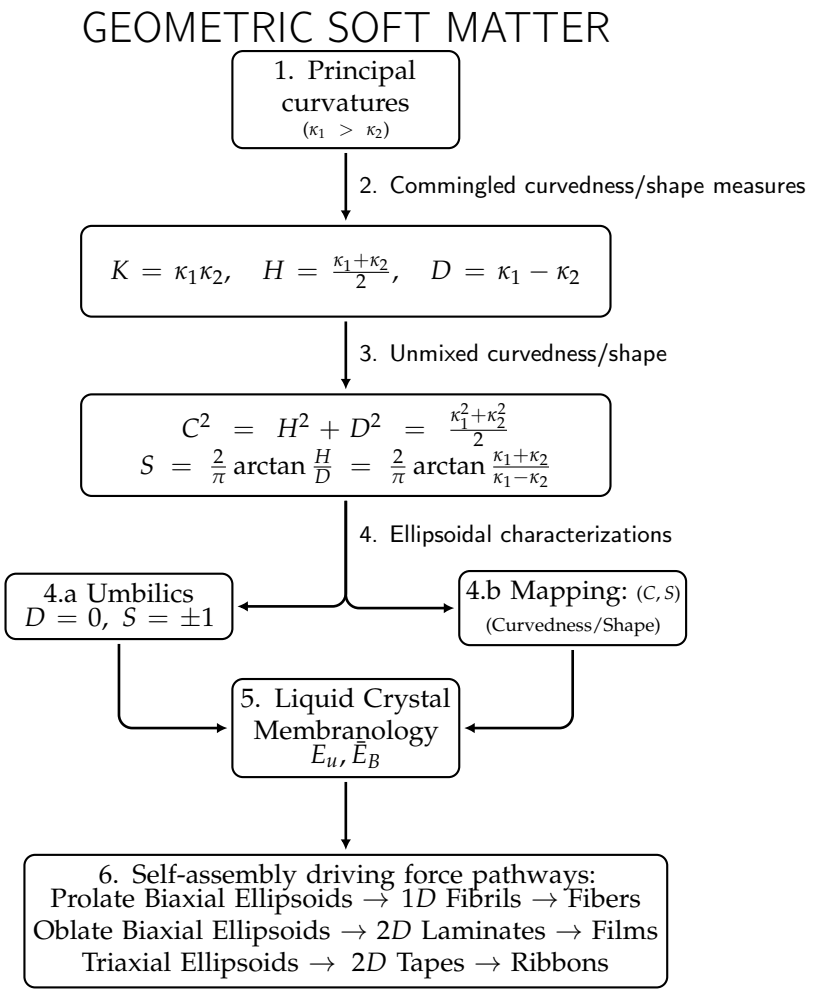

Figure 6. Shape, Size, and Structure $\mathfrak{S}^3$ approach for the global and local study of confined geometries. Special application to soft matter, and self-assembly.

3. Results and Discussion

In this section, we present and discuss the results that follow the workflow described in Section 1 and Figure 7. We first introduce the general framework that links the global to the local parameterization using a shape-structure Monge patch to localize three general cases from Table 1 which follow a constant-volume restriction as form of level-set curves of Eq 4.

In this paper we differentiate shape class and shape anisotropy. Shape class is defined by the eccentricity ratio $m = \frac{e_2}{e_1}$ where $0+ < m < \infty$; example $m = 1$ is a prolate ellipsoid. On the other hand, shape anisotropy is defined by specific values of the eccentricities e_1, e_2; for example the shape anisotropy of a prolate ellipsoid can change by changing e_1, e_2 while maintaining the same value of m ($m = 1$).

In general there are three processes involving shape anisotropy and size:

1. Constant volume- variable shape anisotropy (e.g., biaxial oblate ellipsoid -to-triaxial ellipsoids-to-biaxial prolate ellipsoid)
2. Variable volume- constant shape anisotropy (e.g., expansion of a sphere, expansion of a prolate ellipsoid of given e_1 and e_2).
3. Variable volume-variable shape anisotropy (e.g., shrinking a sphere into a fibril).

In the present paper we focus on process 1 and 3 and leave process 2 for future work.

Subsequently, the global form of the representative cases is mapped into and analyzed using the commingled (H, K) curvedness/shape measures, as they are key descriptors of the unmixed (C, S) curvedness/shape measures. Finally, we map the global parameterization and umbilics energy to show extreme instances of the three cases in Table 1, thus creating a curvature energy chart to help

 doi:10.20944/preprints202604.2051.v1

characterize and identify key shape/curvedness-dependent phenomena (e.g., soft matter self-assembly and self-organization).

Figure 4 shows the global parameterization (e_1, e_2)-space. From this foundational global shape results, we move to various local results in Figures 4-5. Figure 8, Figure 9, and Figure 6 show the local parameterization of the biaxial oblate, biaxial prolate and triaxial ellipsoids with (e_1, e_2) values corresponding to the constant volume case listed in Table 1, Eq 4, and highlighted in Figure 4 ($A \leftrightarrow B \leftrightarrow C$). Figure 10, Figure 11, and Figure 12 show six representative $(C, S)-$maps for the biaxial oblate, biaxial prolate and triaxial shapes, respectively. Figure 5 shows the umbilic energy E_u in Eq as a function of (e_1, e_2) eccentricities.

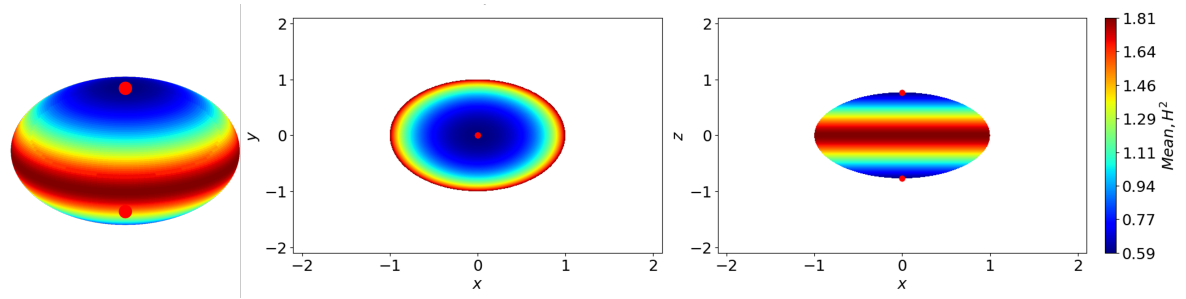

(**a**)

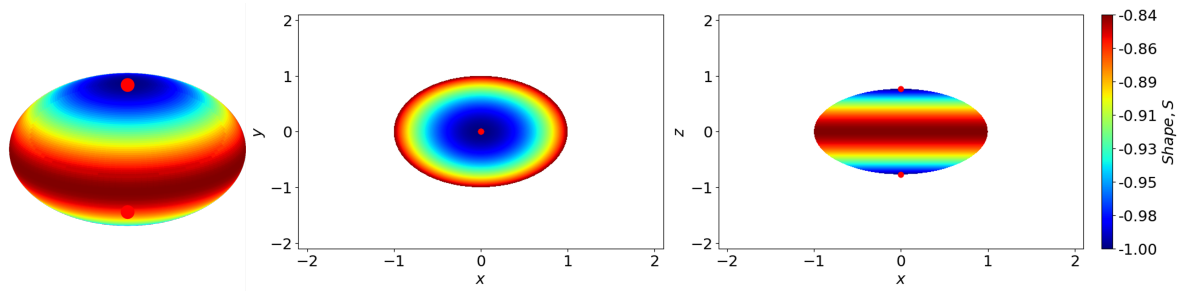

(**b**)

Figure 7. $3D$, top and side views of an oblate surface case $e_1 = 0, e_2 \approx 0.64$ with heatmaps of curvature: mean curvature H^2 and shape coefficient S. Both umbilical points with $+1$ charge are located with a red marker. (**a**) The scale of the squared mean curvature H^2 is color-coded. (**b**) The scale of the shape coefficient S is color-coded.

Preprints.org (www.preprints.org) | NOT PEER-REVIEWED | Posted: 29 April 2026 doi:10.20944/preprints202604.2051.v1

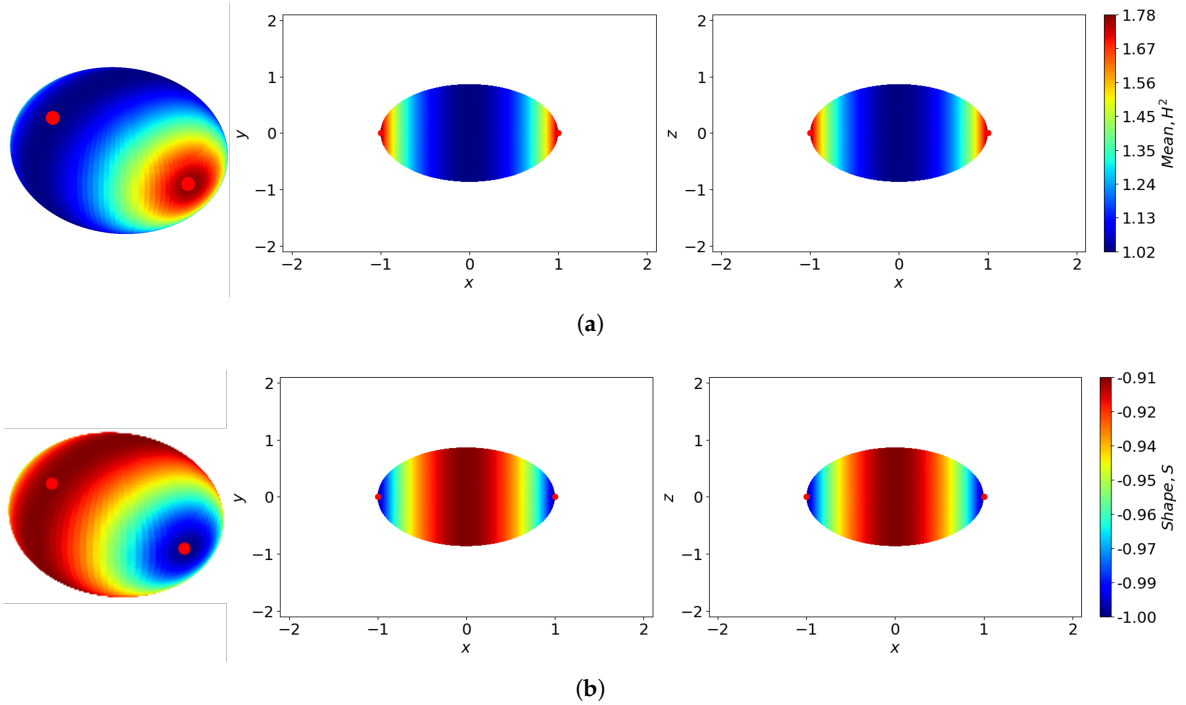

(**a**)

(**b**)

Figure 8. $3D$, top and side views of a prolate surface case $e_1 = 0, e_2 \approx 0.5$ with heatmaps of curvature: mean curvature H^2 and shape coefficient S. Both umbilical points with $+1$ charge are identified with a red marker. (**a**) The scale of the squared mean curvature H^2 is color-coded. (**b**) The scale of the shape coefficient S is color-coded.

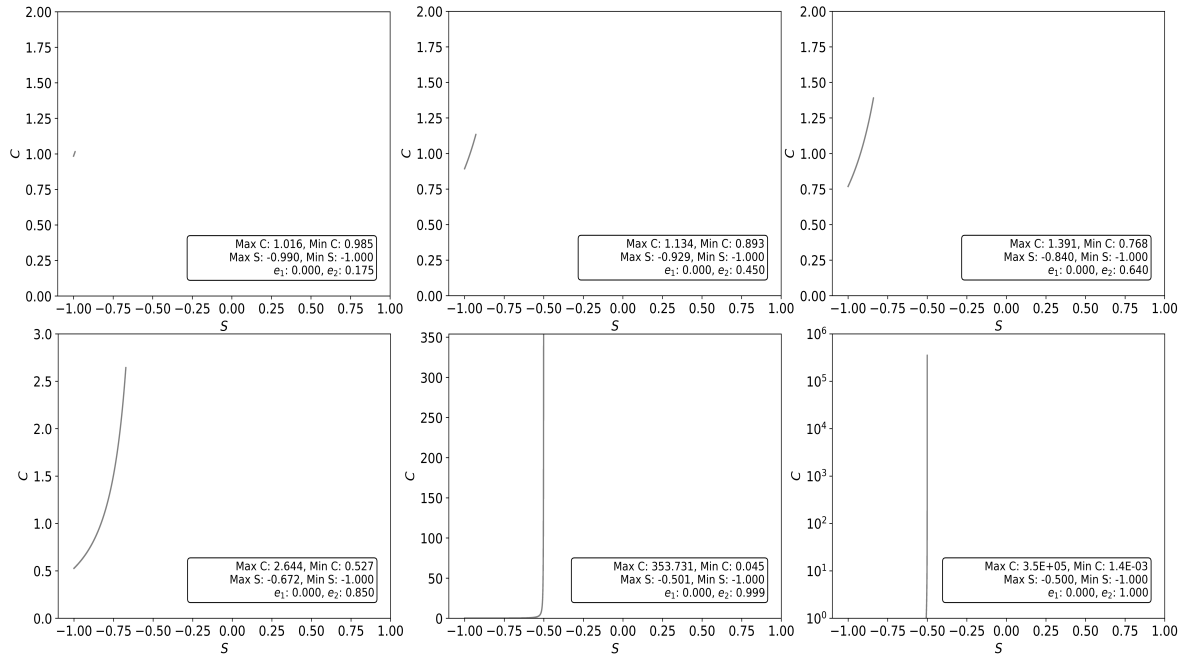

Figure 9. Casorati Curvature (C) and Shape coefficient (S) (Curvedness/Shape) mappings for different oblate ellipsoids as the second eccentricity increases $(e_1 = 0, e_2 \to 1)$, including the oblate case depicted in Figure 8. Data in each panel includes representative information: maximum and minimum values of C, S and their eccentricities e_1, e_2. The panel progression follows a left-to-right, row-by-row.

 doi:10.20944/preprints202604.2051.v1

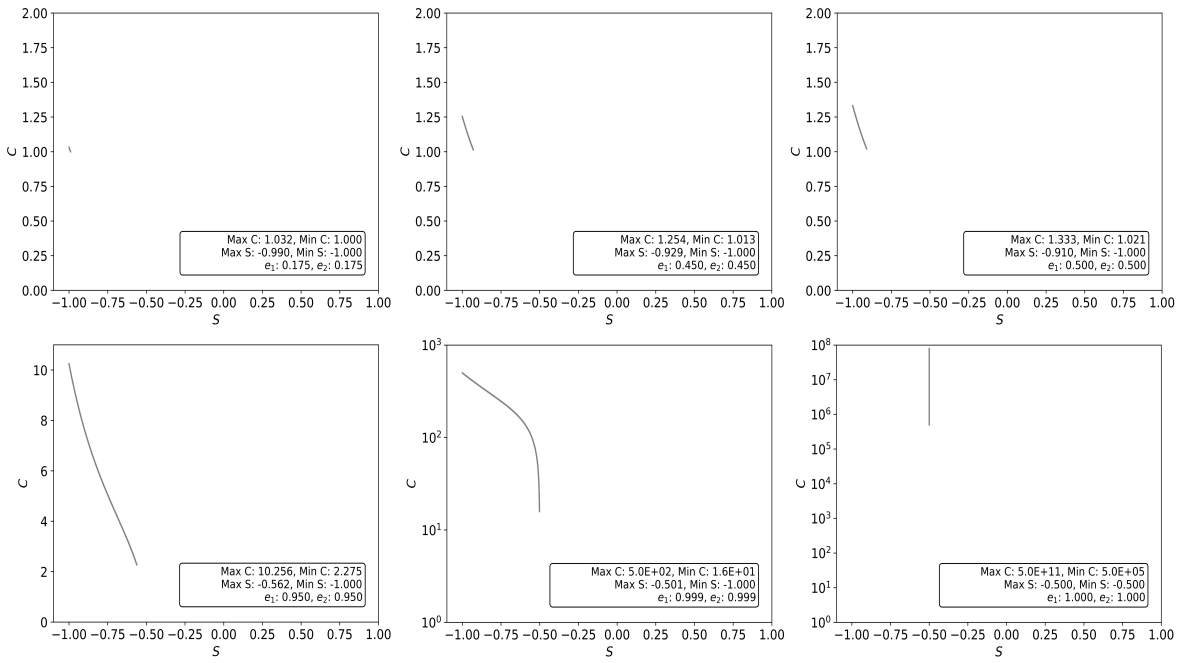

Figure 10. Casorati Curvature (C) and Shape coefficient (S) (Curvedness/Shape) mappings for different prolate ellipsoids as the eccentricities increase $(e_1 = e_2 \to 1)$, including the prolate case shown in Figure 9. Data in each panel includes representative information: maximum and minimum values of C, S and their eccentricities e_1, e_2. The panel progression follows a left-to-right, row-by-row.

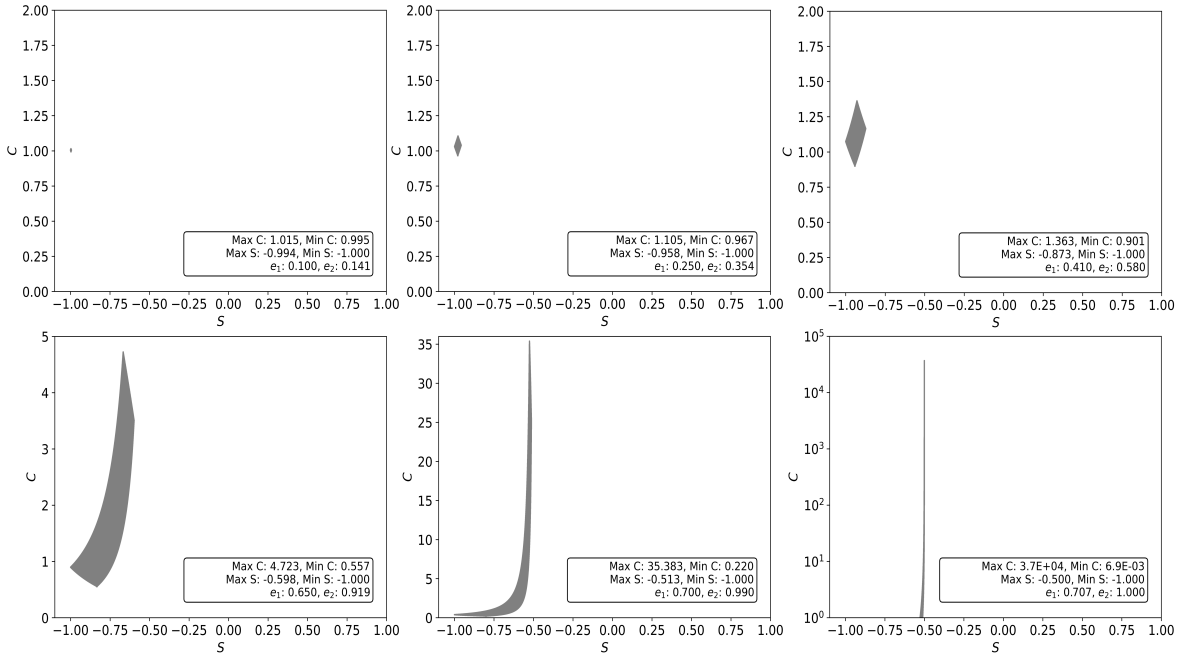

Figure 11. Casorati Curvature (C) and Shape coefficient (S) (Curvedness/Shape) mappings for different triaxial ellipsoids as the eccentricities increase $(e_2 = \sqrt{2}e_1, e_1 \to 1/\sqrt{2})$, and included the generic triaxial case in Figure 6. Annotation in each panel includes representative information of each particular case: maximum and minimum values for both C, S and the eccentricities e_1, e_2 used to compute them. The panel progression follows a left-to-right, row-by-row approach.

3.1. Prolate and Oblate Biaxial Ellipsoids: Global Shape to Local Mapping of Curvedness/Shape

Figure 8 and Figure 9 show the $3D$ and $2D$ views of: (a) the shape coefficient S; and (b) the squared mean curvature H^2. Clear observable bands of different curvature levels follow the minimum curvature lines (see Figure A2-A3) for both biaxial cases in Figure 8(b) and Figure 9(b). Note that the

 doi:10.20944/preprints202604.2051.v1

oblate ellipsoids in Figure 8(a) and Figure 8(b) are not exactly the same, as the shape bands on the surface in case (a) do not follow the same curvature tendency in (b). We can also observe a trade off in the curvature levels between the oblate and prolate cases, where the umbilics are located.

When comparing the curvature in the prolate and oblate biaxial cases (Figure 8(a) and Figure 9(a)), the prolate(oblate) has lower(higher) curvature in the equatorial(polar) regions. Biaxial ellipsoids display two $(+1)$ umbilics at the poles. For prolates(oblates), the umbilics have high(low) curvature and hence energy.

In contrast, the oblate ellipsoid separates the umbilics from the high curvature equatorial ring. The oblate regime shows the flattening of the surface and the generation of a high-curvature barrier which creates a constriction between both hemispheres. This curvature distribution, low in the poles and high in the equator, is compelling for systems where the design requires restriction of particle motion between the upper and lower half surfaces [51].

On the other hand, the shape coefficient S for both cases (in Figure 8(b) and Figure 9(b)) retains the characterizing behavior which locates the umbilics at the points where the local geometry of the surface behaves more like sphere i.e., $S = -1, D = 0, \kappa_1 = \kappa_2$. As consequence, the shape coefficient offers effective characterization techniques of the surface and location of the umbilics, thus complementing the analysis with the curvature energy levels for the study and tuning of curvature-dependent material properties [78,94].

Figure 10 and Figure 11 present the curvedness/shape $(C, S)-$maps for the oblate and prolate ellipsoids as the sphere's symmetry is broken into the limiting disk-like and rod-like structures. The key observation is that mapping the local (H, K) geometry distributions into the $(C, S)-$space yields characteristic curves whose slope, line curvature, length, and end points define biaxial ellipsoids for a given eccentricity (e_1, e_2) pair, as follows.

The evolution of the oblate ellipsoid to the disk-like shape (discoidization) in Figure 10 follows monotonic increase with a positive slope of the curvedness/shape line. As the change occurs, this $(C, S)-$curve shifts to values of S closer to the cylindrical limit at $S = -1/2$ where it finally follows the constant shape behavior with varying curvature. The Casorati extrema range from low values representing the local flat geometry of hemispheres, and the higher values characterize the high curvature equator band seen in Figure 8.

Similarly, the evolution of the prolate case into the fibrillar or rod-like shape (fibrillization) in Figure 11 shows a curvedness/shape line with an increasing negative slope as its behavior follows the constant shape tendency at $S \to -1/2$. However, and contrary to the oblate ellipsoid, the Casorati curvature values do not reach values as low as the minimum (planar case $(C \approxeq 0)$ and the maximum values are higher at the poles than those at the high curvature equatorial ring of the oblate case. In partial summary, in the $(C, S)-$space, the transformation of a sphere into a disk is described by the emergence of L shape and the transformation of a sphere into a fiber by an inverted hockey stick.

3.2. Generic Triaxial Ellipsoid: Global Shape to Local Mapping of Curvedness/Shape

Figure 6 show the local parameterization of a representative case in the general triaxial ellipsoid interval listed in Table 1.

Figure 12 shows the curvedness/shape $(C, S)-$maps for a range of shapes as the sphere's symmetry is broken into the limiting spheroid-like structures that compose the triaxial ellipsoid spectrum. Figure 12 shows how the spherical point $(S = -1, C = 1)$ maps to a range of triaxial ellipsoids areas that represent generic spheroidal shapes(spheroidization). As the change occurs, this closed $(C, S)-$area initially grows in both directions following the prolate and oblate cases followed, creating a small diamond with vertices delimitated by the extrema of the Casorati curvature and shape coefficient values. As the area increases there is a clear quadratic tendency with an axisymmetry on the Casorati axis. For the highest values the eccentricity pair e_1, e_2 can reach for the triaxial case, the surface possesses characteristic behavior for the oblate and prolate: (i) a clear flat geometry region that shows umbilic presence and concentrates the lowest values of the shape coefficient; and (ii) a high-curvature region with the lowest shape coefficient values as seen for the poles of the prolate shape. The last panel

 doi:10.20944/preprints202604.2051.v1

shows the same peak as the prolate and oblate cases, where the system tends to the constant shape behavior.

The results of the generic triaxial ellipsoids are useful for systems with curvature-driven pattern formation, like active surfaces [50]. Interestingly, in the context of nuclear surface, these sphere-like points represent singularities [120] that may characterize instances where rotational levels in nuclei are of special interest. Some initial assumptions involve the representation of the nucleus by defining a triaxial ellipsoid [121], and more recently where some findings show that certain nuclear interactions yield a variation of the ellipsoid of revolution defined by a low potential energy when compared to complete spheroidal nuclei [122,123].

4. Applications for Liquid and Soft Matter Drops and Capsules

The local and global multiscale ellipsoid characterizations have many applications across length scales shown in Fig 3. Here we discuss two contributions to soft matter physics: (1) intrinsic and extrinsic processes involving umbilics on ellipsoidal domains, and (2) curvature driven self-assembly driving forces for films, ribbons, and fiber geometries.

4.1. Application 1: Umbilic Energy (E_u)

Figure 5 shows an umbilic energy E_u landscape as a function of the (e_1, e_2) eccentricities represented in Eq 37. For each of the three general ellipsoids in Table 1, a limiting case is depicted and marked: a sphere at the origin; the general triaxial ellipsoid; the oblate ellipsoid; and the prolate ellipsoid.

The (e_1, e_2) parameterization allows any biaxial or triaxial ellipsoid to become a sphere with larger volume than the original shape by just decreasing one eccentricity. This growth process terminates in a sphere and starts with rod-like, disk-like, or triaxial ellipsoids. In this (e_1, e_2) shape-space, every case with non-constant curvature moves along a curve towards the sphere at the origin $e_1 = e_2 = 0$. In addition to spheroidization we can capture fibrillization and discoidization by a $\min - \max(e_1 = 0, e_2 = 1)$, or a $\max - \min(e_1 = e_2 = 1)$ eccentricity changes and impose the umbilic energy change with the fibrillization(discoidization) with E_u increase(decrease). The trade off in this evolution processes are analogues of the strain, flattening and constriction of confined structures and the shape changes in vesicles with dominating bending curvature [89,109,124].

We observe four limiting cases evaluated in Figure 5 describing a shape evolution processes (see Sections 3.1-3.2) and listed here as:

- Spheroidization $e_2 > e_1, e_1 \to 0, e_2 \to 0$
- Discoidization $e_1 = 0, e_2 \to 1$
- $2D$ Ellipsoidization $0 < e_1 < 1,\ e_2 = 1$
- Fibrillization $e_1 = e_2 \to 1$

This enables the characterization of phenomena sensitive to change in shape, structure, and even size (e.g., droplet, membranes and microstructure evolution [52,89,124,125]), discussed in Section 4.2.

Firstly, spheroidization encompasses a whole transitional interval between the full biaxial oblate and biaxial prolate ellipsoids and represents the decrease of eccentricities towards zero: $e_2 > e_1, e_1 \to 0, e_2 \to 0$. As the name implies, the process represents inflation towards a spherical drop. Depending on the initial state in the (e_1, e_2) triangle, spheroidization generates: a local maximum in E_u (generic triaxial path); a monotonic decrease in E_u (generic triaxial path); a monotonic decreases in E_u (prolate path); or a monotonic increase in E_u (oblate path). The umbilic curvature energy of the general triaxial case represented by the cyan curve in Figure 5 shows a monotonic increase until it decreases following the tendency demarked by the oblate (magenta) case. This dual behavior represents the transitional nature of this triaxial shape, including their curvature and umbilics. There is a tradeoff between the metastable quaternary umbilical charge (four $+1/2$ umbilics) and the stabilization that may occur due to the creation of saddle-like curvature regions (green patches in case II, star marker) reducing the energy of the surface, and analogous to free energy-based models included in Section 2.4.

 doi:10.20944/preprints202604.2051.v1

The discoidization regime $(e_1 = 0, e_2 \to 1)$ is characterized by the lowest umbilic curvature energy E_u, as it was shown in Figure 8 where the highest curvature band corresponds to the equatorial ring, farthest from the umbilic points. This change in shape and structure is analogous to the continuous stretching of membranes with constant surface and volume [89], which only deforms the vesicles, not leading to budding. The location of the umbilics is the origin $x = y = z = 0$.

The 2D ellipsoidization emerges when moving away from the sphere (e_1) along the generalized triaxial ellipsoid line towards: $e_2 = \sqrt{2}e_1$, $e_1 \to 1/\sqrt{2}$. The location of the two umbilics is:

$$x = \pm a\sqrt{\frac{1}{2}}, \quad y = 0, \quad z = 0$$

and is the geometric mean of the fiber $(x = a/2)$ and the disc $(x = 0)$ umbilics.

Finally, in the fibrillization regime the umbilic energy E_u is concentrated right at the poles, which is where the umbilical points $(x = \pm a/2)$ and the highest curvature coincide. The characteristic geometry and high mean curvature at these points may be useful for studying and processing soft matter tactoids. There are some instances that have shown how the coupling of anistropy through orientational ordering and highly curved points can aid in relevant curvature-dependent vesicle membrane processes (i.e., budding and fusion) [52,126–130] positioning it as a highly active shape. Thus, characterizing and mapping the energy across all geometrical space proves useful in the tuning of ellipsoidal tactoids and vesicles with curvature-dependent and ordering-dependent phenomena with focus on change in shape, size and structure.

4.2. Application 2: Curvature-Driven Self-Assembly Driving Force of Ellipsoidal Membrane Structures

This section presents an application of the methods, principles, and trends of global and local geometric modelling of ellipsoids to colloidal self-assembly of liquids, liquid crystals, and soft matter. As this is an immense area of research with myriad applications, the scope of the section is restricted to phenomena captured in Sections 3.1-4.1 and no additional models, theories, and mechanisms driven by the geometry bending elasticity driving force. Hence, the aim is to identify equilibrium self-assembly driving force mechanisms driven by the geometry bending elasticity driving force. Competition, cooperation, and comparisons with other self-assembly mechanisms are not discussed in this section. The analysis assumes that the elastic membrane wrapping the drop is stable under all shape changes. As usual, the self-assembly is described by various orientational and positional order parameters, but the focus of this work is the resulting overall $3D$ shape and not the specific positional and orientational order of the primary packing units i.e., circles, ellipses and needles(see Figure 13). Capsules, encapsulated droplets, membrane liquid crystal drops [101] can be described by colloidal ellipsoids whose surfaces have bending and torsion elasticity.

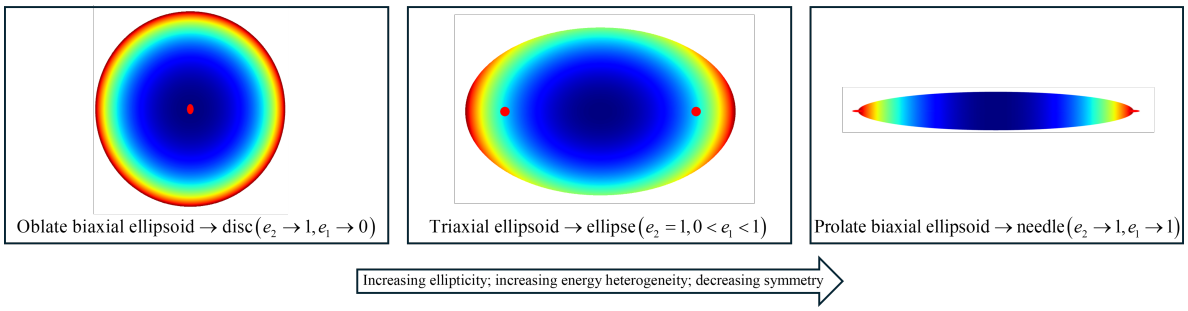

Figure 12. Geometry and bending energy distributions in Eq 36 at high eccentricities. The energy $\bar{E}_B$ is color-coded with low (blue) to high (red) values. The three panels show the top view $(x, y$-plane) of each case. The umbilics are denoted as red markers.

Among the different types of anisotropy relevant to self-assembly, the aspect ratio proves to be a powerful yet simple way to study self-assembly driving force pathways [131,132]. The global shape diagram in 4 shows that at high eccentricity $e_2 \to 1$ the geometric anisotropy is large, and

 doi:10.20944/preprints202604.2051.v1

disks, ellipses, and needle shapes emerge. In practice, these shapes can be approximated by subjecting membrane capsules to high deformation rate biaxial (oblate biaxial), planar (triaxial), and uniaxial (prolate biaxial) extensional flows [133].

The computational results from Eq 36 and presented in Figure 13 characterizing the bending energy distribution $\bar{E}_B$ and the umbilic energy E_u under high eccentricity $(e_2 \to 1)$ biaxial oblate, biaxial prolate, and triaxial ellipsoids show that the geometry of the highest energy locations are shown in Figure 13.

Figure 13 shows by varying an eccentricity ratio m and by approaching critical values that: (i) biaxial oblates become disks with uniform high bending energy on the edge $(m \to \infty)$, (ii) triaxial ellipsoids become ellipses with high energy around the vertices along the longest axis and lower energy around the covertices along the shortest axis $(m = \sqrt{2})$, and (iii) biaxial prolate become rods with the end points having the highest bending energy $(m \to 1)$. Thus, as the eccentricity e_1 increases, the high energy circle (left), becomes elliptical arcs (middle), and finally two end-points (right) showing the connection between bending energy and symmetry breaking, thus expecting m to change under thermodynamic and dissipative processes.

The shape and energy distribution of Figure 13 points to the following self-assembly driving force cascade in Figure 14.

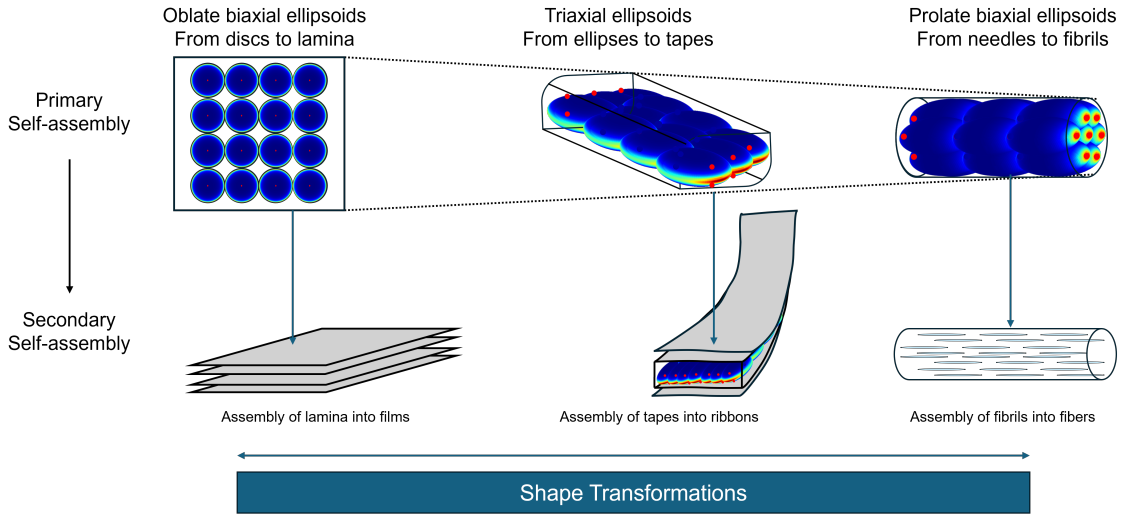

Figure 13. Geometry-bending energy of primary(secondary) directed self-assembly driving force pathways for films(laminates), ribbons(tapes) and fibers(fibril).

The driving force is for overall shapes that minimize the total bending of the assembly, which can be reduced by contacts between high energy packing units. The high energy disks form laminates and the laminates can stack up in the third direction. The narrower tape packed ellipses can stack and form ribbons. The fibrils can form fibers by assembling with a given axial direction.

Finally, the curvature distribution of prolates is consistent with end-cap charged ellipsoidal molecules which self-assemble into a type of fibrillar or rod-like structure with high aspect ratios [109, 126]. Such high energy regions have been registered in other systems with conserved and non-conserved order parameters [134] and in experiments where oil-water interfaces and substrates with ellipsoidal shapes induced a high curvature hotspot at the poles acting as endpoints for the assembly of migrating particles [135]. In contrast, the curvature distribution of the oblates, low in the poles, and high in the equator, limiting case in Section 4.1 (see case III, square marker in Figure 5), shows behavior with charged surface might promote edge-on ordering as in films [45] and adsorption of discs in water-oil interfaces using their circular face [136]. In partial summary, curvature distribution supports the notion of fibrillar(film) self-assembly driving forces for prolates(oblates). As mentioned above, other mechanisms and processes may cooperate or compete with the bending curvature self-assembly driving force identified here. The purpose of the present analysis is to characterize the bending

 doi:10.20944/preprints202604.2051.v1

curvature self-assembly "driving force" and not a colloidal self-assembly process with attractive, repulsive, short-range, and long-range interactions.

5. Conclusions

In this paper, we developed and implemented a novel computational geometrical methodology with differential geometry concepts for the study of the ubiquitous ellipsoidal shape. This approach extends the understanding and complements studies used across different fields with clear symmetry breaking component and/or curvature-dependent phenomena (e.g., topology, soft matter defects and confined structures, determination of material properties).

We have followed the steps and sections introduced in Section 2 and Figure 7 to present a comprehensive geometric modelling framework. Table 4 lists key results that characterize each of these sections. Importantly, the table shows the direct connection between the global eccentricities, the point/lines/areas in the curvedness/shape plane, and the number and charge of umbilics, which taken together offer guidelines for targeted ellipsoidal self-assembly driving force.

Table 4. Characteristic component of the three ellipsoidal cases analyzed in Section 3.

Symmetry Breaking	Case	Global Parameterization	Local Parameterization	Umbilics Number, Charge	Primary Self-assembly Driving Force (Assembly Pathway Endpoint)
Sphere	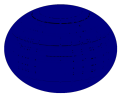	$e_1 = e_2 = 0$	(C, S) maps to a point	Every point behaves like an umbilic	
Biaxial Prolate	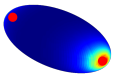	$e_1 = e_2 \in (0, 1]$	(C, S) maps to a curve	$2, \ +1$	$1D$ needle fibril (Fibers)
Biaxial Oblate	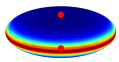	$e_1 = 0, e_2 \in (0, 1]$	(C, S) maps to a curve	$2, \ +1$	$2D$ disk laminate (Films)
Generic Triaxial	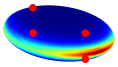	$e_2 = \sqrt{2}e_1 \in (0, 1]$	(C, S) maps to a surface	$4, \ +1/2$	$2D$ ellipse tape (Ribbons)

The novelty and significance of the results and predictions are as follows:

I Global description of ellipsoids. The global parameterization was used to characterize isochoric and shape invariant pathways (see Section 2.1), in ways that separate size, and global shape.

II Local analysis of curvedness/shape for ellipsoidal surfaces. The local parameterization of the surface was carried out using the global parameterization to map the classical and commingled curvedness/shape measures of the surface into two Monge-like patches that portray the unmixed curvedness and shape for the spectra of ellipsoids considered (see Sections 3.1-3.2), again separating two measures.

III Curvature energy landscape. A novel definition of curvature-based energy landscape which maps critical behavior of ellipsoidal shapes in Section 4.1 bridging together the local and global parameterizations.

IV Shape transformation pathways. The geometric bending energy modeling was applied to curvature-driven self-assembly driving force of disk-, ellipse-, and needle-shaped capsules.

 doi:10.20944/preprints202604.2051.v1

Pathways to promote film, ribbon, and fiber formation was identified (Figures 8, Figure 9 and Figure 3.2).

Author Contributions: DUZC and ADR contributed to the conception of the study and analysis of the results. DUZC performed all the computations and prepared figures and bibliography. ADR, NMDC and MJH contributed to the conceptualization and supervision of this paper. All authors contributed to the manuscript revision and read and approved the submitted version.

Funding: This work was supported by the Fonds de Recherche du Québec (FRQNT) (2021-PR-284991) the Natural Science and Engineering Research Council of Canada (NSERC) (#223086). DUZC thanks Consejo Nacional de Humanidades, Ciencia y Tecnología (CONAHCYT) (853563), and McGill Engineering Doctoral Award (MEDA) scholarships for financial support

Institutional Review Board Statement: Not applicable.

Informed Consent Statement: Not applicable.

Data Availability Statement: Data related to this work will be made available by request to the authors. Requests to access the datasets should be directed to the correspondence author.

Acknowledgments: This research was enabled, in part, by support provided by Calcul Quebec (calculquebec.ca), and the Digital Research Alliance of Canada (alliancecan.ca).

Conflicts of Interest: The authors declare no conflicts of interest.

Abbreviations

The following abbreviations are used in this manuscript:

0D	Zero dimensions
1D	One dimension
2D	Two dimensions
3D	Three dimensions
LC	Liquid crystal
LCM	Liquid crystal membranology
LOC	Lines of curvature

Appendix A. Ellipsoidal Parameterizations

This section goes over the parameterization used for describing the ellipsoidal surfaces in this paper in Section 2. It includes the differential geometry treatment to them e.g., first and second fundamental forms coefficients.

Appendix A.1. Constraints and Restrictions

Let the semi-axes of the ellipsoid be a major axis, and (b, c) intermediate and minor axes respectively, with the following restriction:

$$a \geq b \geq c \tag{A1}$$

$$e_1 = \sqrt{1 - \frac{b^2}{a^2}}, \qquad e_2 = \sqrt{1 - \frac{c^2}{a^2}} \tag{A2}$$

where (e_1, e_2) are the widely used eccentricities. Therefore

$$b = a\sqrt{1 - e_1^2}, \qquad c = a\sqrt{1 - e_2^2} \tag{A3}$$

this is just possible if $z > 0$.

In this form, the volume can be described using the eccentricities

 doi:10.20944/preprints202604.2051.v1

$$V = \frac{4}{3}\pi a^3\sqrt{1-e_1^2}\sqrt{1-e_2^2} \tag{A4}$$
$$\bar{V}^2 = 1 - e_1^2 1 - e_2^2 \tag{A5}$$
$$\bar{V}^2 = 1 - e_2^2 - e_1^2 + e_1^2 e_2^2 \tag{A6}$$
$$e_2 = \sqrt{\frac{\bar{V}^2 + e_1^2 - 1}{e_1^2}} \tag{A7}$$

knowing that $a \geq b \geq c$

$$a\sqrt{1-e_1^2} \geq a\sqrt{1-e_2^2} \tag{A8}$$
$$1 - e_1^2 \geq a1 - e_2^2 \tag{A9}$$
$$e_1^2 \leq e_2^2 \tag{A10}$$
$$0 \leq e_1 \leq e_2 \leq 1 \tag{A11}$$

With this parameterization we can define two general cases for the biaxial ellipsoid of revolution: the biaxial oblate and the biaxial prolate. We consider a third case by introducing the arithmetic mean square sum between two axes following the interval in Eq A1 so that:

$$b^2 = \frac{a^2 + c^2}{2} \tag{A12}$$
$$\tag{A13}$$

with Eq A13 and Eq A3 we obtain:

$$2a^2\left(1 - e_1^2\right) = a^2 + a^2\left(1 - e_2^2\right) \tag{A14}$$
$$1 - e_1^2 = 1 - e_2^2/2 \tag{A15}$$
$$e_1^2 = e_2^2/2 \tag{A16}$$
$$e_2 = \sqrt{2}e_1 \tag{A17}$$

Appendix A.2. Cartesian Parameterization

In this section, we develop the first fundamental and second fundamental forms using the vector $\mathbf{Y}(x, y)$, for a given ellipsoidal parametric equation $\mathbf{M}(x, y, z)$.

 doi:10.20944/preprints202604.2051.v1

$$\mathbf{M} = \mathbf{M}(z, x, y) \tag{A18}$$

$$\frac{z^2}{c^2} + \frac{x^2}{a^2} + \frac{y^2}{b^2} = 1 \tag{A19}$$

$$z = c\sqrt{1 - \frac{x^2}{a^2} - \frac{y^2}{b^2}} \tag{A20}$$

considering only the positive root $\frac{x^2}{a^2} + \frac{y^2}{b^2} \leq 1, (a, b) \geq 0$ (A21)

$$\mathbf{Y} = \mathbf{Y}(x, y) \tag{A22}$$

$$\mathbf{Y}(x, y) = \left(c\sqrt{1 - \frac{x^2}{a^2} - \frac{y^2}{b^2}}, x, y\right) \tag{A23}$$

$$\frac{\partial \mathbf{Y}}{\partial x} = \left(-\frac{c^2 x}{a^2 z}, 1, 0\right) \tag{A24}$$

$$\frac{\partial \mathbf{Y}}{\partial y} = \left(-\frac{c^2 y}{b^2 z}, 0, 1\right) \tag{A25}$$

$$\frac{\partial^2 \mathbf{Y}}{\partial x^2} = \left(-\frac{c^2}{z a^2}\left(1 + \frac{c^2 x^2}{a^2 z^2}\right), 0, 0\right) = \left(-\frac{c^2(b^2 - y^2)}{a^2 b^2 z^3}, 0, 0\right) \tag{A26}$$

$$\frac{\partial^2 \mathbf{Y}}{\partial y^2} = \left(-\frac{c^2}{z b^2}\left(1 + \frac{c^2 y^2}{b^2 z^2}\right), 0, 0\right) = \left(-\frac{c^2(a^2 - x^2)}{a^2 b^2 z^3}, 0, 0\right) \tag{A27}$$

$$\frac{\partial^2 \mathbf{Y}}{\partial x \partial y} = \left(-\frac{c^4 x y}{a^2 b^2 z^3}, 0, 0\right) \tag{A28}$$

$$\mathbf{n} = \frac{\partial \mathbf{Y}}{\partial x} \times \frac{\partial \mathbf{Y}}{\partial y} = \left(1, \frac{c^2 x}{z a^2}, \frac{c^2 y}{z b^2}\right) \tag{A29}$$

$$n = \sqrt{1 + \frac{c^4 x^2}{z^2 a^4} + \frac{c^4 y^2}{z^2 b^4}} = \sqrt{1 + \left(\frac{\partial Y_1}{\partial x}\right)^2 + \left(\frac{\partial Y_1}{\partial y}\right)^2} \tag{A30}$$

$$\hat{\mathbf{n}} = \frac{\mathbf{n}}{|n|} \tag{A31}$$

For convenience, the elements of the surface metric are renamed with the notation of the first and second fundamental coefficients:

$$\frac{\partial \mathbf{Y}}{\partial x} \cdot \frac{\partial \mathbf{Y}}{\partial x} = \left(-\frac{c^2 x}{a^2 z} \cdot -\frac{c^2 x}{a^2 z} + 1 \cdot 1 + 0 \cdot 0\right) = \frac{c^4 x^2}{a^4 z^2} + 1 = E \tag{A32}$$

$$\frac{\partial \mathbf{Y}}{\partial y} \cdot \frac{\partial \mathbf{Y}}{\partial y} = \left(-\frac{c^2 y}{b^2 z} \cdot -\frac{c^2 y}{b^2 z} + 0 \cdot 0 + 1 \cdot 1\right) = \frac{c^4 y^2}{b^4 z^2} + 1 = G \tag{A33}$$

$$\frac{\partial \mathbf{Y}}{\partial x} \cdot \frac{\partial \mathbf{Y}}{\partial y} = \left(-\frac{c^2 x}{a^2 z} \cdot -\frac{c^2 y}{b^2 z} 1 \cdot 0 + 0 \cdot 1\right) = \frac{c^4 x y}{a^2 b^2 z^2} = F \tag{A34}$$

So that the first fundamental form is:

$$\mathbf{g} = \begin{bmatrix} 1 + \left(\frac{\partial \mathbf{Y}}{\partial x}\right)^2 & \left(\frac{\partial \mathbf{Y}}{\partial x} \frac{\partial \mathbf{Y}}{\partial y}\right) \\ \left(\frac{\partial \mathbf{Y}}{\partial x} \frac{\partial \mathbf{Y}}{\partial y}\right) & 1 + \left(\frac{\partial \mathbf{Y}}{\partial y}\right)^2 \end{bmatrix} = \begin{bmatrix} E & F \\ F & G \end{bmatrix} \tag{A35}$$

 doi:10.20944/preprints202604.2051.v1

The second fundamental coefficients are computed by applying the dot product of the vectors coming from the second derivative terms with the unit normal vector $\hat{\mathbf{n}}$:

$$\frac{\partial^2 \mathbf{Y}}{\partial x^2} \cdot \hat{\mathbf{n}} = \frac{c\left(y^2 - b^2\right)}{|n|\sqrt{1 - \frac{x^2}{a^2} - \frac{y^2}{b^2}}\left(a^2(b^2 - y^2) - b^2x^2\right)} = \frac{c^2\left(y^2 - b^2\right)}{nz(a^2(b^2 - y^2) - b^2x^2)} \tag{A36}$$

$$\frac{\partial^2 \mathbf{Y}}{\partial x \partial y} \cdot \hat{\mathbf{n}} = -\frac{cxy}{a^2b^2|n|\left(-\frac{x^2}{a^2} - \frac{y^2}{b^2} + 1\right)^{3/2}} = -\frac{c^4xy}{nz^3a^2b^2} \tag{A37}$$

$$\frac{\partial^2 \mathbf{Y}}{\partial y^2} \cdot \hat{\mathbf{n}} = \frac{c\left(x^2 - a^2\right)}{|n|\sqrt{1 - \frac{x^2}{a^2} - \frac{y^2}{b^2}}\left(a^2(b^2 - y^2) - b^2x^2\right)} = \frac{c^2\left(x^2 - a^2\right)}{nz(a^2(b^2 - y^2) - b^2x^2)} \tag{A38}$$

$$L = -\frac{c^4\left(b^2 - y^2\right)}{nz^3a^2b^2} \tag{A39}$$

$$M = -\frac{c^4xy}{nz^3a^2b^2} \tag{A40}$$

$$N = -\frac{c^4\left(a^2 - x^2\right)}{nz^3a^2b^2} \tag{A41}$$

Appendix A.3. Angular Parameterization

From Eq A18 in spherical coordinates:

$$\frac{r^2\cos^2 u \sin^2 v}{a^2} + \frac{r^2\cos^2 u \sin^2 v}{b^2} + \frac{r^2\cos^2 v}{c^2} = 1 \tag{A42}$$

$$\mathbf{p} = \mathbf{p}(u, v) \tag{A43}$$

$$x = a\cos u \sin v, y = b\sin u \sin v, z = c\cos v \tag{A44}$$

where (u, v) are the polar and the azimuthal angles, respectively.

$$\mathbf{p} = (a\cos u \sin v, b\sin u \sin v, c\cos v) \tag{A45}$$

$$\frac{\partial \mathbf{p}}{\partial u} = (-a\sin u \sin v, b\cos u \sin v, 0) \tag{A46}$$

$$\frac{\partial \mathbf{p}}{\partial v} = (a\cos u \cos v, b\sin u \cos v, -c\sin v) \tag{A47}$$

$$\frac{\partial \mathbf{p}}{\partial u} \cdot \frac{\partial \mathbf{p}}{\partial u} = E = \left(a^2\sin^2 u + b^2\cos^2 u\right)\sin^2 v \tag{A48}$$

$$\frac{\partial \mathbf{p}}{\partial u} \cdot \frac{\partial \mathbf{p}}{\partial v} = F = \left(-a^2 + b^2\right)\sin u \sin v \cos u \cos v \tag{A49}$$

$$\frac{\partial \mathbf{p}}{\partial v} \cdot \frac{\partial \mathbf{p}}{\partial v} = G = \left(a^2\cos^2 u + b^2\sin^2 u\right)\cos^2 v + c^2\sin^2 v \tag{A50}$$

 doi:10.20944/preprints202604.2051.v1

$$\mathbf{n} = \frac{\partial \mathbf{p}}{\partial u} \times \frac{\partial \mathbf{p}}{\partial v} = \left(-bc\cos u \sin^2 v, -ac \sin u \sin^2 v, -ab \cos v \sin v(\cos^2 u + \sin^2 u)\right) \tag{A51}$$

$$\mathbf{n} = \frac{\partial \mathbf{p}}{\partial u} \times \frac{\partial \mathbf{p}}{\partial v} = \left(-bc\cos u \sin^2 v, -ac \sin u \sin^2 v, -ab \cos v \sin v\right) \tag{A52}$$

$$n = \sqrt{(ab\cos v \sin v)^2 + (bc\cos u \sin^2 v)^2 + (ac \sin u \sin^2 v)^2} \tag{A53}$$

$$n = \sin v \sqrt{a^2b^2\cos^2 v + c^2 \sin^2 v\left(a^2 \sin^2 u + b^2 \cos^2 u\right)} = \sqrt{EG - F^2} \tag{A54}$$

$$\hat{\mathbf{n}} = \mathbf{n}/|n| \tag{A55}$$

$$\frac{\partial^2 \mathbf{p}}{\partial u^2} = (-a\cos u \sin v, -b \sin u \sin v, 0) \tag{A56}$$

$$\frac{\partial^2 \mathbf{p}}{\partial u \partial v} = (-a\sin u \cos v, b \cos u \cos v, 0) \tag{A57}$$

$$\frac{\partial^2 \mathbf{p}}{\partial v^2} = (-a\cos u \sin v, -b \sin u \sin v, -c \cos v) \tag{A58}$$

$$\frac{\partial^2 \mathbf{p}}{\partial u^2} \cdot \hat{\mathbf{n}} = L = \left(\frac{abc \sin^3 v}{n}\right) = \frac{abc \sin^2 v}{\sqrt{a^2b^2\cos^2 v + c^2 \sin^2 v\left(a^2 \sin^2 u + b^2 \cos^2 u\right)}} \tag{A59}$$

$$\frac{\partial^2 \mathbf{p}}{\partial u \partial v} \cdot \hat{\mathbf{n}} = M = 0 \tag{A60}$$

$$\frac{\partial^2 \mathbf{p}}{\partial v^2} \cdot \hat{\mathbf{n}} = N = \left(\frac{abc \sin v}{n}\right) = \frac{abc}{\sqrt{a^2b^2\cos^2 v + c^2 \sin^2 v\left(a^2 \sin^2 u + b^2 \cos^2 u\right)}} \tag{A61}$$

Appendix B. Parallel Surfaces

Parallel surfaces, used in liquid crystal membranology [99–108] are defined by a zero curl of the outward unit normal k.

$$\nabla \times \mathbf{k} = \mathbf{0} \tag{A62}$$

Parallel surfaces are characterized by the curl-free condition:

$$(\mathbf{k} \cdot \nabla)\mathbf{k} = \mathbf{0} \tag{A63}$$

which states that along the normal direction, the unit vector $\mathbf{k}$ is constant as shown in Figure A1.

 doi:10.20944/preprints202604.2051.v1

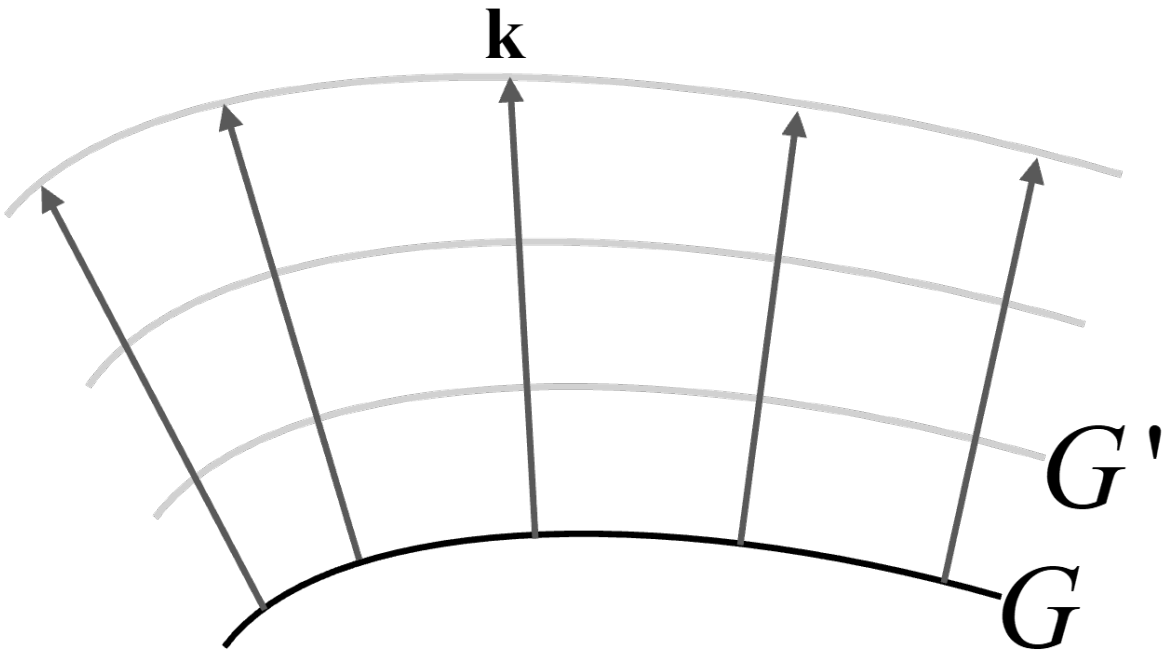

Figure A1. Parent surface G with its family of parallel surfaces G' and their outward unit normal $\mathbf{k}$.

Since G and G' are parallel, the direction of $\mathbf{k}$ at both surfaces is equal. Selecting a parent surface to the family using a decomposition of the $3D$ gradient we find:

$$\nabla\mathbf{k} = (\mathbf{I} - \mathbf{kk}) \cdot \nabla\mathbf{k} + \mathbf{kk} \cdot \nabla\mathbf{k} = \mathbf{I}_s \cdot \nabla\mathbf{k} + \mathbf{k}(\mathbf{k} \cdot \nabla\mathbf{k}) = \nabla_s\mathbf{k} + \mathbf{k}(\mathbf{k}\nabla\mathbf{k}) \tag{A64}$$

where the surface identity tensor is $\mathbf{I}_s - \mathbf{I} - \mathbf{kk}$, and ∇_s is the surface gradient. Using the definition of the symmetric curvature tensor

$$\nabla_s\mathbf{k} = -\mathbf{B} \tag{A65}$$

and substituting Eq A65 and Eq A63 into Eq A64 we find

$$\nabla\mathbf{k} = \nabla_s\mathbf{k} = -\mathbf{B} \tag{A66}$$

Using the definition of curl using the alternator tensor ε, we find:

$$\nabla \times \mathbf{k} = -\nabla \cdot \varepsilon \cdot \mathbf{k} = +\varepsilon : \nabla\mathbf{k} = \varepsilon : \mathbf{B} = \mathbf{0} \tag{A67}$$

since $\mathbf{B}$ is symmetric, it agrees with Eq A62.

Appendix C. Lines of curvature and Umbilics in Bi-axial and triaxial ellipsoids

This section includes the derivation and the results of the lines of curvature for the biaxial and triaxial ellipsoids and their pattern around the umbilics discussed in Section 2.3.

Considering $a > b > c > 0$, the coordinates of the umbilic points of an ellipsoid are:

$$x = \pm a\sqrt{\frac{a^2 - b^2}{a^2 - c^2}} \tag{A68}$$

$$y = 0 \tag{A69}$$

$$z = \pm c\sqrt{\frac{b^2 - c^2}{a^2 - c^2}} \tag{A70}$$

 doi:10.20944/preprints202604.2051.v1

or in terms of the eccentricities

$$x = \pm a\sqrt{\frac{e_1^2}{e_2^2}} \tag{A71}$$

$$y = 0 \tag{A72}$$

$$z = \pm a\sqrt{1-e_2^2}\sqrt{\frac{e_1^2}{e_2^2}} \tag{A73}$$

It is known that the principal curvatures κ_1, κ_2 are eig($\mathbf{B}$), thus from Eq 14:

$$\det(\mathbf{B} - \kappa_i \mathbf{I}) = 0 \tag{A74}$$

$$\mathbf{B} - \kappa_i \mathbf{I} = \frac{1}{\det \mathbf{g}} \begin{bmatrix} LG - MF - \kappa & -LF + ME \\ MG - NF & -MF + NE - \kappa \end{bmatrix} \tag{A75}$$

$$\det(\mathbf{B} - \kappa_i \mathbf{I}) = \frac{1}{\det \mathbf{g}} \left[\kappa^2 - (GL - 2MF + EN)\kappa + (F^2 - EG)(M^2 - LN)\right] \tag{A76}$$

$$\det(\mathbf{B} - \kappa_i \mathbf{I}) = \frac{1}{\det \mathbf{g}} \left[\kappa^2 - \operatorname{tr}\mathbf{B}\,\kappa + \det \mathbf{B}\right] = 0 \tag{A77}$$

$$\kappa_{1,2} = \frac{-(-\operatorname{tr}\mathbf{B})}{2} \pm \sqrt{\left(\frac{-\operatorname{tr}\mathbf{B}}{2}\right)^2 - 4\frac{\det \mathbf{B}}{4}} \tag{A78}$$

$$\kappa_{1,2} = H \pm \sqrt{H^2 - K} = H \pm D \tag{A79}$$

The definition for the mean and Gaussian curvatures can be written as a function of the (C, S):

$$H = C \sin\left(\frac{S\pi}{2}\right) \tag{A80}$$

$$K = C^2 \sin^2\left(\frac{S\pi}{2}\right) - C^2 \cos^2\left(\frac{S\pi}{2}\right) = -C^2 \cos(S\pi) \tag{A81}$$

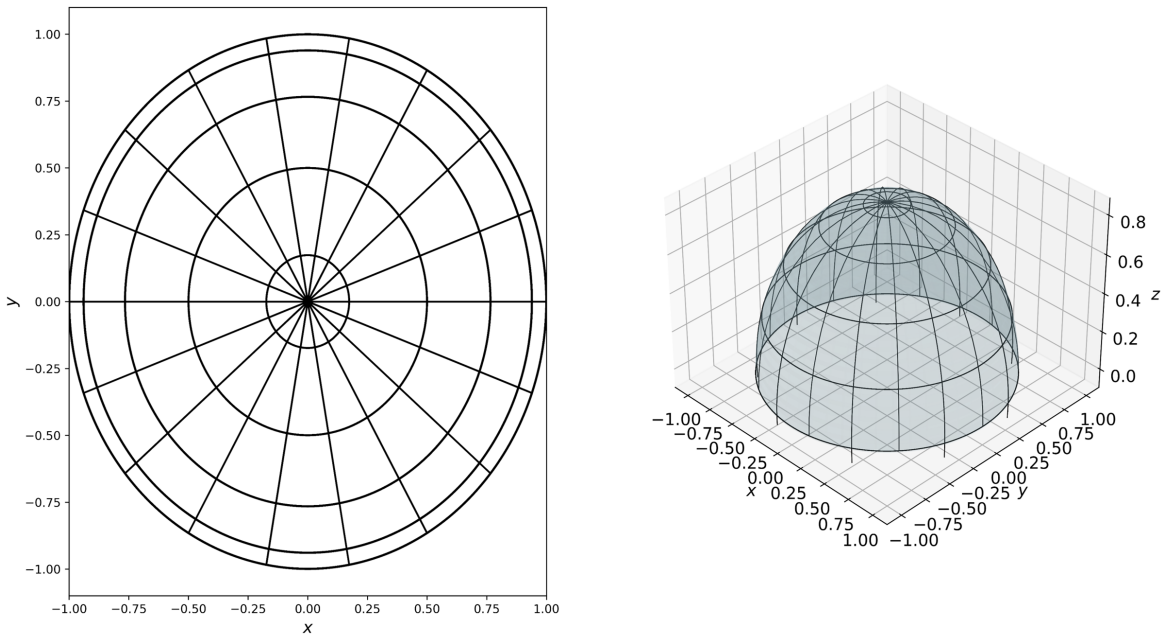

Figure A2. Lines of curvature network of the biaxial oblate ellipsoid $e_1 = 0, e_2 = 0.5$. Only one half is included for visualization purposes. The pattern shows non-generic umbilics with a $+1$ charge at the poles.

 doi:10.20944/preprints202604.2051.v1

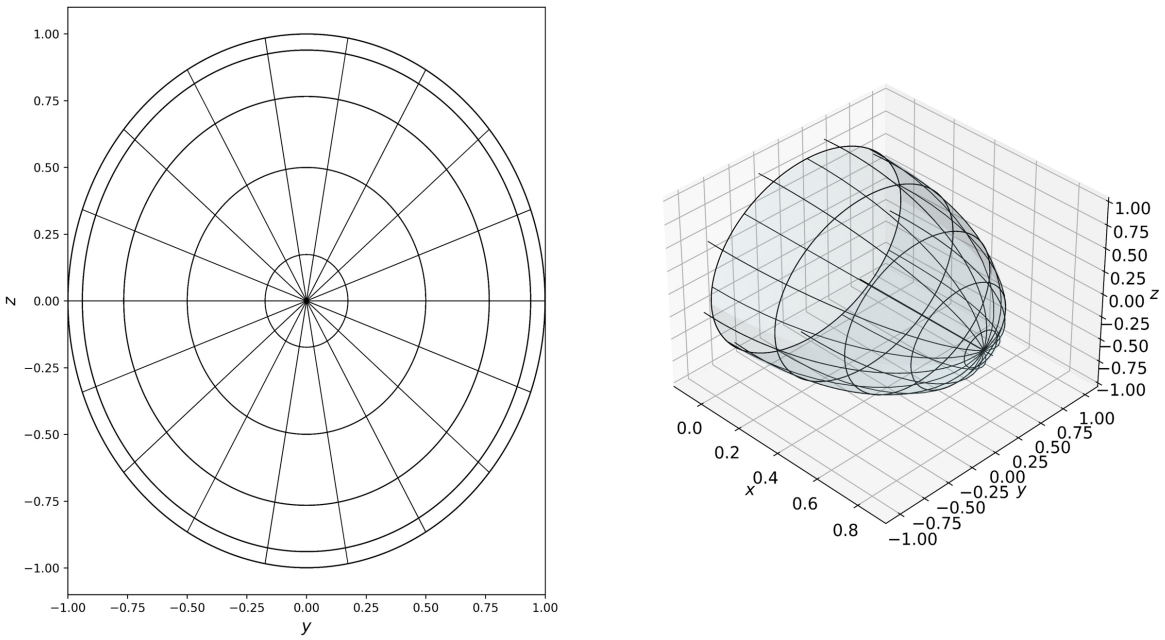

Figure A3. Lines of curvature network of the biaxial prolate ellipsoid $e_1 = e_2 = 0.5$. Only one half is included for visualization purposes. The pattern shows non-generic umbilics with a $+1$ charge at the poles.

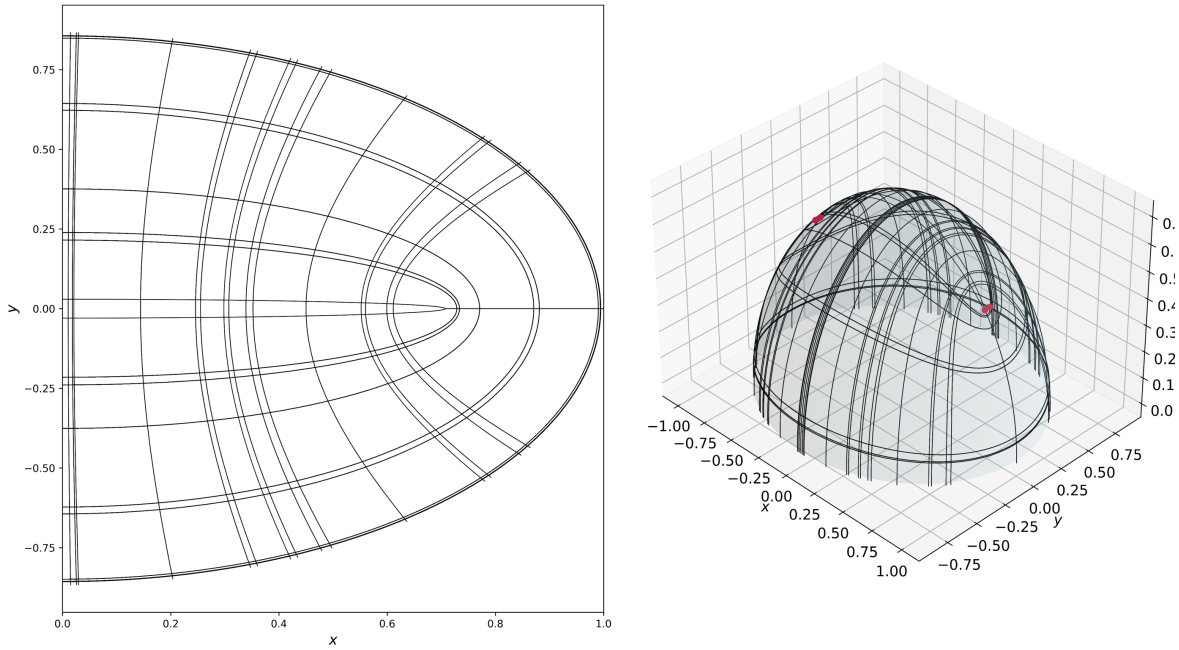

Figure A4. Lines of curvature network of the general triaxial ellipsoid $e_1 = 0.5, e_2 = e_1\sqrt{2}$. Only one half is included for visualization purposes. The lemon-like pattern shows umbilics (red markers) with a $+1/2$ charge.

References

1. Ulusoy, U. A Review of Particle Shape Effects on Material Properties for Various Engineering Applications: From Macro to Nanoscale. *Miner* **2023**, *13*, 91. https://doi.org/ARTN9110.3390/min13010091.
2. Adams, J.M. Particle-Size and Shape Effects in Materials Science - Examples from Polymer and Paper Systems. *Clay Miner* **1993**, *28*, 509–530. https://doi.org/DOI10.1180/claymin.1993.028.4.03.
3. Decuzzi, P.; Godin, B.; Tanaka, T.; Lee, S.Y.; Chiappini, C.; Liu, X.; Ferrari, M. Size and shape effects in the biodistribution of intravascularly injected particles. *J Control Release* **2010**, *141*, 320–327. https://doi.org/10.1016/j.jconrel.2009.10.014.

 doi:10.20944/preprints202604.2051.v1

4. Ankamwar, B., Size and Shape Effect on Biomedical Applications of Nanomaterials. In *Biomedical Engineering - Technical Applications in Medicine*; Hudak, R.; Penhaker, M.; Majernik, J., Eds.; IntechOpen: London, 2012; book section Chapter 4. https://doi.org/10.5772/46121.
5. Babayevska, N.; Przysiecka, L.; Iatsunskyi, I.; Nowaczyk, G.; Jarek, M.; Janiszewska, E.; Jurga, S. ZnO size and shape effect on antibacterial activity and cytotoxicity profile. *Sci Rep* **2022**, *12*, 8148. https://doi.org/10.1038/s41598-022-12134-3.
6. Seifert, U.; Berndl, K.; Lipowsky, R. Shape transformations of vesicles: Phase diagram for spontaneous-curvature and bilayer-coupling models. *Phys Rev A* **1991**, *44*, 1182–1202. https://doi.org/10.1103/physreva.44.1182.
7. Krivoshapko, S.N. Tangential developable and hydrodynamic surfaces for early stage of ship shape design. *Ships Offshore Struct* **2022**, *18*, 660–668. https://doi.org/10.1080/17445302.2022.2062165.
8. Krivoshapko, S.N. Research on general and axisymmetric ellipsoidal shells used as domes, pressure vessels, and tanks. *Applied Mechanics Reviews* **2007**, *60*, 336–355. https://doi.org/10.1115/1.2806278.
9. Tang, Y.H.; Zhang, J.; Wang, F.; Zhao, X.L.; Wang, M.L. Buckling performance of ellipsoidal pressure hulls with stepwise wall thicknesses. *Ocean Eng* **2023**, *284*, 115165. https://doi.org/ARTN11516510.1016/j.oceaneng.2023.115165.
10. Tangbanjongkij, C.; Chucheepsakul, S.; Jiammeepreecha, W. Large displacement analysis of ellipsoidal pressure vessel heads using the fundamental of differential geometry. *Int J Pres Ves Pip* **2019**, *172*, 337–347. https://doi.org/10.1016/j.ijpvp.2019.04.001.
11. Zingoni, A.; Enoma, N. On the strength and stability of elliptic toroidal domes. *Eng Struct* **2020**, *207*, 110241. https://doi.org/ARTN11024110.1016/j.engstruct.2020.110241.
12. Wang, Z.; Servio, P.; Rey, A.D. Pattern formation, structure and functionalities of wrinkled liquid crystal surfaces: A soft matter biomimicry platform. *Front Soft Matter* **2023**, *3*, 1123324.
13. Rofouie, P.; Pasini, D.; Rey, A.D. Nanostructured free surfaces in plant-based plywoods driven by chiral capillarity. *Colloid Interfac Sci* **2014**, *1*, 23–26. https://doi.org/10.1016/j.colcom.2014.06.003.
14. Guerra, A.; Wang, Z.; Mathews, S.; Rey, A.D.; De France, K. Periodic Feature Characterization in Nanostructured Surfaces and Emulsions. *Langmuir* **2025**, *41*, 25230–25241. https://doi.org/10.1021/acs.langmuir.5c02320.
15. Wang, Z.; Servio, P.; Rey, A.D. Cholesteric liquid crystal roughness models: from statistical characterization to inverse engineering. *Soft Matter* **2025**, *21*, 4517–4532. https://doi.org/10.1039/d5sm00121h.
16. Wang, Z.; Servio, P.; Rey, A.D. Structure and Pattern Formation in Biological Liquid Crystals: Insights From Theory and Simulation of Self-Assembly and Self-Organization. *Front Soft Matter* **2022**, *2*. https://doi.org/10.3389/frsfm.2022.904069.
17. Rising, A.; Harrington, M.J. Biological Materials Processing: Time-Tested Tricks for Sustainable Fiber Fabrication. *Chem Rev* **2023**, *123*, 2155–2199. Rising, Anna Harrington, Matthew J eng Research Support, Non-U.S. Gov't Review 2022/12/13 Chem Rev. 2023 Mar 8;123(5):2155-2199. doi: 10.1021/acs.chemrev.2c00465. Epub 2022 Dec 12., https://doi.org/10.1021/acs.chemrev.2c00465.
18. Liu, X.; Zhang, Y.; Fernandes, M.; Volbeda, F.; Parisi, D.; Portale, G.; Es Sayed, J.; Kamperman, M. Spider Silk Inspired Processing of Liquid Crystalline Complex Coacervates. *ACS Macro Lett* **2026**, *15*, 76–82. https://doi.org/10.1021/acsmacrolett.5c00630.
19. H, R.A.; Ojagh, S.M.A.; Jafari, A.; Zhan, X.; Sprules, T.; Poulhazan, A.; Savoji, H.; Hendricks, A.G.; van de Ven, T.G.M.; Harrington, M.J. Mistletoe- and Mussel-Inspired Fabrication of Hierarchically Structured Protein-Cellulose Scaffolds From Biomolecular Condensates. *Adv Mater* **2026**, *n/a*, e20827. https://doi.org/10.1002/adma.202520827.
20. Baer, A.; Schmidt, S.; Haensch, S.; Eder, M.; Mayer, G.; Harrington, M.J. Mechanoresponsive lipid-protein nanoglobules facilitate reversible fibre formation in velvet worm slime. *Nat Commun* **2017**, *8*, 974. Baer, Alexander Schmidt, Stephan Haensch, Sebastian Eder, Michaela Mayer, Georg Harrington, Matthew J eng Research Support, Non-U.S. Gov't England 2017/10/19 Nat Commun. 2017 Oct 17;8(1):974. doi: 10.1038/s41467-017-01142-x., https://doi.org/10.1038/s41467-017-01142-x.
21. Fudge, D.S.; Schorno, S.; Ferraro, S. Physiology, biomechanics, and biomimetics of hagfish slime. *Annu Rev Biochem* **2015**, *84*, 947–967. Fudge, Douglas S Schorno, Sarah Ferraro, Shannon eng Review 2014/12/24 Annu Rev Biochem. 2015;84:947-67. doi: 10.1146/annurev-biochem-060614-034048. Epub 2014 Dec 12., https://doi.org/10.1146/annurev-biochem-060614-034048.
22. Almohammadi, H.; Khadem, S.A.; Bagnani, M.; Rey, A.D.; Mezzenga, R. Shape and structural relaxation of colloidal tactoids. *Nat Commun* **2022**, *13*, 2778. https://doi.org/10.1038/s41467-022-30123-y.

 doi:10.20944/preprints202604.2051.v1

23. Mezzenga, R.; Seddon, J.M.; Drummond, C.J.; Boyd, B.J.; Schroder-Turk, G.E.; Sagalowicz, L. Nature-Inspired Design and Application of Lipidic Lyotropic Liquid Crystals. *Adv Mater* **2019**, *31*, e1900818. https://doi.org/10.1002/adma.201900818.
24. Lin, D.; Almohammadi, H.; Zhao, Y.; Mezzenga, R. Remodeling and self-healing of individual amyloid tactoids via multiphoton absorption. *Nat Commun* **2025**, *17*, 254. https://doi.org/10.1038/s41467-025-66954-8.
25. Li, T.; Ilhamsyah, D.; Tai, B.; Shen, Y. Functional Biomaterials Derived from Protein Liquid-Liquid Phase Separation and Liquid-to-Solid Transition. *Adv Mater* **2025**, *37*, e2414703. https://doi.org/10.1002/adma.202414703.
26. Soulé, E.R.; Abukhdeir, N.M.; Rey, A.D. Thermodynamics, Transition Dynamics, and Texturing in Polymer-Dispersed Liquid Crystals with Mesogens Exhibiting a Direct Isotropic/Smectic-A Transition. *Macromol* **2009**, *42*, 9486–9497. doi: 10.1021/ma901569y, https://doi.org/10.1021/ma901569y.
27. Khadem, S.A.; Rey, A.D. Nucleation and growth of cholesteric collagen tactoids: A time-series statistical analysis based on integration of direct numerical simulation (DNS) and long short-term memory recurrent neural network (LSTM-RNN). *J Colloid Interface Sci* **2021**, *582*, 859–873.
28. O'Keefe, M.; Garcia, J.; Rwakabuba, A.J.; Otchy, T.M.; Beller, D.A.; Gharbi, M.A. Templated self-assembly of gold nanoparticles in smectic liquid crystals confined at 3D printed curved surfaces. *Nanoscale* **2025**, *17*, 20351–20364. https://doi.org/10.1039/d4nr02539c.
29. Beller, D.A.; Gharbi, M.A.; Liu, I.B. Shape-controlled orientation and assembly of colloids with sharp edges in nematic liquid crystals. *Soft Matter* **2015**, *11*, 1078–1086. https://doi.org/10.1039/c4sm01910e.
30. Gharbi, M.A.; Liu, I.B.; Luo, Y.; Serra, F.; Bade, N.D.; Kim, H.N.; Xia, Y.; Kamien, R.D.; Yang, S.; Stebe, K.J. Smectic Gardening on Curved Landscapes. *Langmuir* **2015**, *31*, 11135–11142. https://doi.org/10.1021/acs.langmuir.5b02508.
31. Serra, F.; Gharbi, M.A.; Luo, Y.M.; Liu, I.B.; Bade, N.D.; Kamien, R.D.; Yang, S.; Stebe, K.J. Curvature-Driven, One-Step Assembly of Reconfigurable Smectic Liquid Crystal "Compound Eye" Lenses. *Adv Opt Mat* **2015**, *3*, 1287–1292. https://doi.org/10.1002/adom.201500153.
32. Vitral, E.; Leo, P.H.; Vinals, J. Role of Gaussian curvature on local equilibrium and dynamics of smectic-isotropic interfaces. *Phys Rev E* **2019**, *100*, 032805. https://doi.org/10.1103/PhysRevE.100.032805.
33. Mewis, J.; Wagner, N.J. *Colloidal suspension rheology*; Cambridge University Press: Cambridge (UK), 2012.
34. Yazdani-Ahmadabadi, H.; Yu, K.; Khoddami, S.; D, F.F.; Yeh, H.H.; Luo, H.D.; Moskalev, I.; Wang, Q.; Wang, R.; Grecov, D.; et al. Robust Nanoparticle-Derived Lubricious Antibiofilm Coating for Difficult-to-Coat Medical Devices with Intricate Geometry. *ACS Nanosci Au* **2023**, *3*, 67–83. https://doi.org/10.1021/acsnanoscienceau.2c00040.
35. Zakani, B.; Grecov, D. Effect of ultrasonic treatment on yield stress of highly concentrated cellulose nanocrystalline (CNC) aqueous suspensions. *Carbohydr Polym* **2022**, *291*, 119651. https://doi.org/10.1016/j.carbpol.2022.119651.
36. Noroozi, N.; Grecov, D. Numerical simulation of three-dimensional flow-induced microstructure in a simplified prosthetic hip joint with nematic liquid crystal lubricant. *Rheologica Acta* **2014**, *53*, 457–465. https://doi.org/10.1007/s00397-014-0773-3.
37. Bazilevsky, A.V.; Kornev, K.G. Classification of axisymmetric shapes of droplets on fibers. Could non-wettable fibers support axisymmetric droplets? *Phys Fluids* **2023**, *35*. https://doi.org/10.1063/5.0151950.
38. Mu, W.; Ou-Yang, Z.C.; Cao, J. The stability of spherocyte membranes: Theoretical study. *Europhys Lett* **2019**, *128*, 38001. https://doi.org/Artn3800110.1209/0295-5075/128/38001.
39. Lane, L.A. Physics in nanomedicine: Phenomena governing the performance of nanoparticles. *Appl Phys Rev* **2020**, *7*. https://doi.org/Artn01131610.1063/1.5052455.
40. Toy, R.; Peiris, P.M.; Ghaghada, K.B.; Karathanasis, E. Shaping cancer nanomedicine: the effect of particle shape on the in vivo journey of nanoparticles. *Nanomed* **2014**, *9*, 121–134. https://doi.org/10.2217/nnm.13.191.
41. Perera, T.; Mallawaarachchi, S.; Premaratne, M. Chiral Plasmonic Ellipsoids: An Extended Mie-Gans Model. *J Phys Chem Lett* **2021**, *12*, 11214–11219. https://doi.org/10.1021/acs.jpclett.1c03144.
42. Ilca, S.L.; Sun, X.; El Omari, K.; Kotecha, A.; de Haas, F.; DiMaio, F.; Grimes, J.M.; Stuart, D.I.; Poranen, M.M.; Huiskonen, J.T. Multiple liquid crystalline geometries of highly compacted nucleic acid in a dsRNA virus. *Nature* **2019**, *570*, 252–256. https://doi.org/10.1038/s41586-019-1229-9.

 doi:10.20944/preprints202604.2051.v1

43. Abdali, Z.; Renner-Rao, M.; Chow, A.; Cai, A.; Harrington, M.J.; Dorval Courchesne, N.M. Extracellular Secretion and Simple Purification of Bacterial Collagen from Escherichia coli. *Biomacromolecules* **2022**, *23*, 1557–1568. https://doi.org/10.1021/acs.biomac.1c01191.
44. Alloyeau, D.; Ricolleau, C.; Mottet, C.; Oikawa, T.; Langlois, C.; Le Bouar, Y.; Braidy, N.; Loiseau, A. Size and shape effects on the order-disorder phase transition in CoPt nanoparticles. *Nat Mater* **2009**, *8*, 940–946. https://doi.org/10.1038/nmat2574.
45. Aguilar Gutierrez, O.F.; Rey, A.D. Theory and Simulation of Cholesteric Film Formation Flows of Dilute Collagen Solutions. *Langmuir* **2016**, *32*, 11799–11812. https://doi.org/10.1021/acs.langmuir.6b03443.
46. Zamora Cisneros, D.U.; Wang, Z.; Dorval Courchesne, N.M.; Harrington, M.J.; Rey, A.D. Geometric modeling of phase ordering for the isotropic–smectic A phase transition. *Front Soft Matter* **2024**, *4*, 1359128.
47. Abbena, E.; Salamon, S.; Gray, A. *Modern differential geometry of curves and surfaces with Mathematica*, 3rd ed.; Chapman and Hall/CRC: New York (NY), 2017; pp. 385–430,593–638.
48. Patrikalakis, N.M.; Maekawa, T. *Shape interrogation for computer aided design and manufacturing*; Vol. 15, Springer, 2002; pp. 231–264.
49. Kurik, M.V.; Lavrentovich, O. Defects in liquid crystals: homotopy theory and experimental studies. *Sov Phys Uspekhi* **1988**, *31*, 196–224.
50. Alaimo, F.; Kohler, C.; Voigt, A. Curvature controlled defect dynamics in topological active nematics. *Sci Rep* **2017**, *7*, 5211. https://doi.org/10.1038/s41598-017-05612-6.
51. Ehrig, S.; Ferracci, J.; Weinkamer, R.; Dunlop, J.W.C. Curvature-controlled defect dynamics in active systems. *Phys Rev E* **2017**, *95*, 062609. https://doi.org/10.1103/PhysRevE.95.062609.
52. Kurioz, P.; Mesarec, L.; Iglic, A.; Kralj, S. Assembling of Topological Defects at Neck-Shaped Membrane Parts. *Phys Status Solidi A* **2019**, *216*, 1800722. https://doi.org/ARTN180072210.1002/pssa.201800722.
53. Penič, S.; Mesarec, L.; Fošnarič, M.; Mrówczyńska, L.; Hägerstrand, H.; Kralj-Iglič, V.; Iglič, A. Budding and Fission of Membrane Vesicles: A Mini Review. *Front Phys* **2020**, *8*. https://doi.org/10.3389/fphy.2020.00342.
54. Otsuka, T.; Tsunoda, Y.; Shimizu, N.; Utsuno, Y.; Abe, T.; Ueno, H. Prevailing triaxial shapes in atomic nuclei and a quantum theory of rotation of composite objects. *Eur Phys J A* **2025**, *61*, 126. https://doi.org/ARTN12610.1140/epja/s10050-025-01553-1.
55. Verney, D. History of the concept of nuclear shape. *Eur Phys J* **2025**, *61*, 82. https://doi.org/10.1140/epja/s10050-025-01545-1.
56. Reuther, S.; Voigt, A. Erratum: The interplay of curvature and vortices in flow on curved surfaces. *Multiscale Model Simul* **2018**, *16*, 1448–1453.
57. Nitschke, I.; Voigt, A.; Wensch, J. A finite element approach to incompressible two-phase flow on manifolds. *J Fluid Mech* **2012**, *708*, 418–438. https://doi.org/10.1017/jfm.2012.317.
58. Turner, A.M.; Vitelli, V.; Nelson, D.R. Vortices on curved surfaces. *Rev Mod Phys* **2010**, *82*, 1301–1348. https://doi.org/10.1103/RevModPhys.82.1301.
59. Jaffe, R.L.; Taylor, W. *The physics of energy*; Cambridge University Press: Cambridge (UK), 2018; pp. 299–322.
60. Bennett, C.D.; Ravenhall, D.G. Effect of Curvature on Nuclear Surface-Energy. *Phys Rev C* **1974**, *10*, 2058–2066. https://doi.org/10.1103/PhysRevC.10.2058.
61. Pethick, C.J.; Potekhin, A.Y. Liquid crystals in the mantles of neutron stars. *Phys Lett B* **1998**, *427*, 7–12. https://doi.org/10.1016/S0370-2693(98)00341-4.
62. Ragnarsson, I.; Nilsson, S.G.; Sheline, R.K. Shell Structure in Nuclei. *Phys Rep* **1978**, *45*, 1–87. https://doi.org/10.1016/0370-1573(78)90004-2.
63. Leoni, S.; Fornal, B.; Bracco, A.; Tsunoda, Y.; Otsuka, T. Multifaceted character of shape coexistence phenomena in atomic nuclei. *Prog Part Nucl Phys* **2024**, *139*, 104119. https://doi.org/10.1016/j.ppnp.2024.104119.
64. Pearce, D.J.G. Coupling the topological defect phase to the extrinsic curvature in nematic shells. *Soft Matter* **2022**, *18*, 5082–5088. https://doi.org/10.1039/d2sm00602b.
65. Schimming, C.D.; Vinals, J. Singularity identification for the characterization of topology, geometry, and motion of nematic disclination lines. *Soft Matter* **2022**, *18*, 2234–2244. https://doi.org/10.1039/d1sm01584b.
66. Myers, L.; Swift, C.; Ronning, J.; Angheluta, L.; Vinals, J. A computational study of nematic core structure and disclination interactions in elastically anisotropic nematics. *Soft Matter* **2024**, *20*, 2900–2914. https://doi.org/10.1039/d3sm01616a.
67. Sinha, K.; Graham, M.D. Dynamics of a single red blood cell in simple shear flow. *Phys Rev E Stat Nonlin Soft Matter Phys* **2015**, *92*, 042710. https://doi.org/10.1103/PhysRevE.92.042710.

 doi:10.20944/preprints202604.2051.v1

68. Jan, K.M.; Chien, S. Role of surface electric charge in red blood cell interactions. *J Gen Physiol* **1973**, *61*, 638–654. https://doi.org/10.1085/jgp.61.5.638.
69. Herrera-Valencia, E.E.; Ramírez-Torres, L.A.; Soriano-Correa, C.; Sánchez-Villavicencio, M.L.; Bautista, O.; Hernández-Abad, V.J.; Calderas, F. Effects of multiple relaxation times in the annular flow of pulsatile electro-osmotic flow of a complex biological fluid: blood with low and high cholesterol. *Front Soft Matter* **2024**, *4*. https://doi.org/10.3389/frsfm.2024.1385512.
70. Jehle, F.; Priemel, T.; Strauss, M.; Fratzl, P.; Bertinetti, L.; Harrington, M.J. Collagen Pentablock Copolymers Form Smectic Liquid Crystals as Precursors for Mussel Byssus Fabrication. *ACS Nano* **2021**, *15*, 6829–6838. https://doi.org/10.1021/acsnano.0c10457.
71. Renner-Rao, M.; Clark, M.; Harrington, M.J. Fiber Formation from Liquid Crystalline Collagen Vesicles Isolated from Mussels. *Langmuir* **2019**, *35*, 15992–16001. https://doi.org/10.1021/acs.langmuir.9b01932.
72. Demtröder, W. *Nuclear and Particle Physics*; Springer, 2022; pp. 123–152.
73. Sharma, I. *Shapes and Dynamics of Granular Minor Planets*; Springer, 2017; pp. 95–128.
74. Wang, Z.; Servio, P.; Rey, A.D. Geometry-structure models for liquid crystal interfaces, drops and membranes: wrinkling, shape selection and dissipative shape evolution. *Soft Matter* **2023**.
75. Peng, C.; Guo, Y.; Conklin, C.; Vinals, J.; Shiyanovskii, S.V.; Wei, Q.H.; Lavrentovich, O.D. Liquid crystals with patterned molecular orientation as an electrolytic active medium. *Phys Rev E Stat Nonlin Soft Matter Phys* **2015**, *92*, 052502. https://doi.org/10.1103/PhysRevE.92.052502.
76. Zamora Cisneros, D.U.; Harrington, M.J.; Dorval Courchesne, N.; Rey, A.D. Geometric-Bifurcation Methods for Dual Order-Disorder Transitions: Applications to the Isotropic-to-Smectic A Phase Transformation. *Adv Eng Mater* **2025**, *27*, 2402724. https://doi.org/10.1002/adem.202402724.
77. Renner-Rao, M.; Priemel, T.; Anderson, J.; Jehle, F.; Harrington, M.J. Multiresponsive Liquid Crystal Collagen Guides Mussel Byssus Formation. *Biomacromolecules* **2024**, *25*, 6038–6049. Renner-Rao, Max Priemel, Tobias Anderson, Jack Jehle, Franziska Harrington, Matthew J eng Research Support, Non-U.S. Gov't 2024/08/15 Biomacromolecules. 2024 Sep 9;25(9):6038-6049. doi: 10.1021/acs.biomac.4c00709. Epub 2024 Aug 15., https://doi.org/10.1021/acs.biomac.4c00709.
78. Machon, T.; Alexander, G.P. Umbilic Lines in Orientational Order. *Phys Rev X* **2016**, *6*, 011033. https://doi.org/10.1103/PhysRevX.6.011033.
79. Wang, Z.; Servio, P.; Rey, A. Wrinkling pattern formation with periodic nematic orientation: From egg cartons to corrugated surfaces. *Phys Rev E* **2022**, *105*, 034702.
80. Herrera-Valencia, E.E.; Rey, A.D. Fluctuating Flexoelectric Membranes in Asymmetric Viscoelastic Media: Power Spectrum through Mechanical Network and Transfer Function Models. *Symmetry* **2023**, *15*, 1004. https://doi.org/ARTN100410.3390/sym15051004.
81. Kahraman, O.; Stoop, N.; Müller, M.M. Morphogenesis of membrane invaginations in spherical confinement. *Europhys Lett* **2012**, *97*, 68008. 914md Times Cited:25 Cited References Count:28, https://doi.org/Artn68008 10.1209/0295-5075/97/68008.
82. Reeves, J.P.W.; Rostami, S.; Rammal, M.; Bocan, A.; Lépine, P.; Harrington, M.J.; Durcan, T.M.; Moraes, C. Stress-adaptive biomaterials with tunable yielding architectures regulate organoid morphogenesis. *bioRxiv* **2026**, p. 2026.2001.2029.702625. https://doi.org/10.64898/2026.01.29.702625.
83. Hohenester, U., Particle Plasmons. In *Nano and Quantum Optics*; Hohenester, U., Ed.; Graduate Texts in Physics, Springer International Publishing: Cham, 2020; book section Chapter 9, pp. 207–257. https://doi.org/10.1007/978-3-030-30504-8_9.
84. Sachs, S.; Schmidt, H.; Cierpka, C.; König, J. On the behavior of prolate spheroids in a standing surface acoustic wave field. *Microfluid Nanofluid* **2023**, *27*, 81. https://doi.org/ARTN8110.1007/s10404-023-02690-z.
85. Mitri, F.G. Axisymmetric scattering of an acoustical Bessel beam by a rigid fixed spheroid. *IEEE Trans Ultrason Ferroelectr Freq Control* **2015**, *62*, 1809–1818. https://doi.org/10.1109/TUFFC.2014.006811.
86. Farouki, R.T. On integrating lines of curvature. *Comp Aided Geom Des* **1998**, *15*, 187–192. https://doi.org/ https://doi.org/10.1016/S0167-8396(97)00022-8.
87. Wang, Z.; Servio, P.; Rey, A.D. Rate of entropy production in evolving interfaces and membranes under astigmatic kinematics: Shape evolution in geometric-dissipation landscapes. *Entropy* **2020**, *22*, 909.
88. Aguilar Gutierrez, O.F.; Rey, A.D. Extracting shape from curvature evolution in moving surfaces. *Soft Matter* **2018**, *14*, 1465–1473. https://doi.org/10.1039/C7SM02409F.
89. Vázquez-Montejo, P.; Božič, B.; Guven, J. Equatorial deformation of homogeneous spherical fluid vesicles by a rigid ring. *Phys Rev E* **2025**, *111*, 035411. https://doi.org/10.1103/PhysRevE.111.035411.

 doi:10.20944/preprints202604.2051.v1

90. Maekawa, T.; Wolter, F.E.; Patrikalakis, N.M. Umbilics and lines of curvature for shape interrogation. *Computer Aided Geometric Design* **1996**, *13*, 133–161. https://doi.org/https://doi.org/10.1016/0167-8396(95)00018-6.
91. Koning, V.; Vitelli, V., Crystals and Liquid Crystals Confined to Curved Geometries. In *Fluids, Colloids and Soft Materials: An Introduction to Soft Matter Physics*; Fernandez-Nieves, A.; Manuel Puertas, A., Eds.; Wiley: Hoboken (NJ), 2016; book section 19, pp. 369–386. https://doi.org/10.1002/9781119220510.ch19.
92. Gray, A.; Abbena, E.; Salamon, S., Modern differential geometry of curves and surfaces with Mathematica; Studies in advanced mathematics, Chapman and Hall/CRC: Boca Raton, 2006; chapter Shape and Curvature, pp. 385–430.
93. Do Carmo, M.P. *Differential geometry of curves and surfaces: revised and updated second edition*; Courier Dover Publications: Mineola (NY), 2016.
94. Gharbi, M.A.; Nobili, M.; Blanc, C. Use of topological defects as templates to direct assembly of colloidal particles at nematic interfaces. *J Colloid Interface Sci* **2014**, *417*, 250–255. https://doi.org/10.1016/j.jcis.2013.11.051.
95. Berry, M.V.; Hannay, J.H. Umbilic points on Gaussian random surfaces. *Journal of Physics A: Mathematical and General* **1977**, *10*, 1809. https://doi.org/10.1088/0305-4470/10/11/009.
96. Sander, P.T.; Zucker, S.W. Singularities of Principal Direction Fields from 3-D Images. *Ieee T Pattern Anal Mach Intell* **1992**, *14*, 309–317. https://doi.org/Doi10.1109/34.120326.
97. Porteous, I.R. *Geometric differentiation: for the intelligence of curves and surfaces*, 2nd ed.; Cambridge University Press: Cambridge (UK), 2001; pp. 158–181,198–213,265–285.
98. Gutiérrez, C.; Sotomayor, J.; Garcia, R. Bifurcations of umbilic points and related principal cycles. *J Dyn Differ Equ* **2004**, *16*, 321–346.
99. Rey, A.D. Capillary models for liquid crystal fibers, membranes, films, and drops. *Soft Matter* **2007**, *3*, 1349–1368. https://doi.org/10.1039/b704248p.
100. De Gennes, P.G.; Prost, J. *The physics of liquid crystals*, 2nd ed.; Oxford University Press: New York (NY), 1993.
101. Rofouie, P.; Pasini, D.; Rey, A.D. Morphology of elastic nematic liquid crystal membranes. *Soft Matter* **2017**, *13*, 5366–5380. https://doi.org/10.1039/c7sm00977a.
102. Gelbart, W.M.; Ben-Shaul, A.; Roux, D. *Micelles, membranes, microemulsions, and monolayers*; Springer Science & Business Media: New York, 2012; pp. 251–322.
103. Rey, A.D.; Servio, P.; Herrera-Valencia, E.E. Bioinspired model of mechanical energy harvesting based on flexoelectric membranes. *Phys Rev E Stat Nonlin Soft Matter Phys* **2013**, *87*, 022505. https://doi.org/10.1103/PhysRevE.87.022505.
104. Rofouie, P.; Pasini, D.; Rey, A.D. Multiple-wavelength surface patterns in models of biological chiral liquid crystal membranes. *Soft Matter* **2017**, *13*, 541–545. https://doi.org/10.1039/c6sm02619b.
105. Edwards, D.A.; Wasan, D.T. Surface Rheology II. The Curved Fluid Surface. *J Rheol*, *32*, 447–472. https://doi.org/10.1122/1.549978.
106. Kleman, M.; .; Lavrentovich, O.D. Liquids with conics. *Liq Cryst* **2009**, *36*, 145,347,1085–1099. doi:10.1080/02678290902814718, https://doi.org/10.1080/02678290902814718.
107. Rey, A.D. Liquid crystal models of biological materials and processes. *Soft Matter* **2010**, *6*, 3402–3429. https://doi.org/10.1039/b921576j.
108. Donald, A.M.; Windle, A.H.; Hanna, S. *Liquid crystalline polymers*, 2nd ed.; Cambridge University Press: Cambridge (UK), 2006.
109. Safran, S. *Statistical thermodynamics of surfaces, interfaces, and membranes*; CRC Press: Boca Raton, 2018; p. 178.
110. Marko, J.F.; Siggia, E.D. Bending and Twisting Elasticity of DNA. *Macromol* **1994**, *27*, 981–988. https://doi.org/DOI10.1021/ma00082a015.
111. Adamcik, J.; Mezzenga, R. Amyloid Polymorphism in the Protein Folding and Aggregation Energy Landscape. *Angew Chem Int Ed Engl* **2018**, *57*, 8370–8382. https://doi.org/10.1002/anie.201713416.
112. Jewell, S.A. Living systems and liquid crystals. *Liquid Crystals* **2011**, *38*, 1699–1714. https://doi.org/10.1080/02678292.2011.603846.
113. Rey, A.D. Liquid crystal model of membrane flexoelectricity. *Phys Rev E Stat Nonlin Soft Matter Phys* **2006**, *74*, 011710. https://doi.org/10.1103/PhysRevE.74.011710.
114. Petrov, A.G. *The lyotropic state of matter : molecular physics and living matter physics*; Gordon and Breach Science Publishers: Amsterdam (Netherlands), 1999; pp. 131–242.
115. Guckenberger, A.; Gekle, S. Theory and algorithms to compute Helfrich bending forces: a review. *J Phys Condens Matter* **2017**, *29*, 203001. https://doi.org/10.1088/1361-648X/aa6313.

 doi:10.20944/preprints202604.2051.v1

116. Laradji, M.; Zhu, Y.; Sharma, A.; Spangler, E.J.; Darling, J.F. Ordered nanoparticle self-assembly driven by membrane curvature: computational insights. *Adv Phys-X* **2026**, *11*, 2605083. https://doi.org/Artn2605083 10.1080/23746149.2025.2605083.
117. Virga, E.G. *Variational theories for liquid crystals*; Chapman and Hall/CRC, 2018; pp. 106–172.
118. Kleman, M.; Lavrentovich, O.D. *Soft matter physics: an introduction*; Springer, 2003; pp. 135–169.
119. Campelo, F.; Arnarez, C.; Marrink, S.J.; Kozlov, M.M. Helfrich model of membrane bending: from Gibbs theory of liquid interfaces to membranes as thick anisotropic elastic layers. *Adv Colloid Interface Sci* **2014**, *208*, 25–33. https://doi.org/10.1016/j.cis.2014.01.018.
120. Möller, P.; Sierk, A.J.; Bengtsson, R.; Sagawa, H.; Ichikawa, T. Nuclear shape isomers. *Atomic Data and Nuclear Data Tables* **2012**, *98*, 149–300. https://doi.org/10.1016/j.adt.2010.09.002.
121. Davydov, A.S.; Rostovsky, V.S. Relative Transition Probabilities between Rotational Levels of Non-Axial Nuclei. *Nuclear Physics* **1959**, *12*, 58–68. https://doi.org/Doi10.1016/0029-5582(59)90127-0.
122. Kokkonen, H.; Auranen, K.; Siwach, P.; Arumugam, P.; Briscoe, A.D.; Eeckhaudt, S.; Ferreira, L.S.; Grahn, T.; Greenlees, P.T.; Jones, P.; et al. New proton emitter (188)At implies an interaction unprecedented in heavy nuclei. *Nat Commun* **2025**, *16*, 4985. https://doi.org/10.1038/s41467-025-60259-6.
123. Montes Plaza, A.; Pakarinen, J.; Papadakis, P.; Herzberg, R.D.; Julin, R.; Rodriguez, T.R.; Briscoe, A.D.; Illana, A.; Ojala, J.; Ruotsalainen, P.; et al. Direct measurement of three different deformations near the ground state in an atomic nucleus. *Commun Phys* **2025**, *8*, 8. https://doi.org/10.1038/s42005-024-01928-8.
124. Ramsay, J.G.; Wood, D.S. The geometric effects of volume change during deformation processes. *Tectonophysics* **1973**, *16*, 263–277. https://doi.org/10.1016/0040-1951(73)90015-2.
125. Jiang, Y.; Liang, B.Z.; Xin, S.W.; Shi, L.; Zhang, S.Y.; Zhang, K.; Wang, H.; Yang, Y.; Zhang, L.C. Cyclic Heat Treatment Induced Spheroidization of α Phase in Ti-5Al-3Mo-3V-2Cr-2Zr-1Nb-1Fe Alloy. *Acta Metall Sin-Engl* **2025**, *38*, 1827–1838. https://doi.org/10.1007/s40195-025-01903-4.
126. Crassous, J.J.; Mihut, A.M.; Wernersson, E.; Pfleiderer, P.; Vermant, J.; Linse, P.; Schurtenberger, P. Field-induced assembly of colloidal ellipsoids into well-defined microtubules. *Nat Commun* **2014**, *5*, 5516. https://doi.org/10.1038/ncomms6516.
127. Iglic, A.; Babnik, B.; Bohinc, K.; Fosnaric, M.; Hagerstrand, H.; Kralj-Iglic, V. On the role of anisotropy of membrane constituents in formation of a membrane neck during budding of a multicomponent membrane. *J Biomech* **2007**, *40*, 579–585. https://doi.org/10.1016/j.jbiomech.2006.02.006.
128. Jesenek, D.; Perutkova, S.; Kralj-Iglic, V.; Kralj, S.; Iglic, A. Exocytotic fusion pore stability and topological defects in the membrane with orientational degree of ordering. *Cell Calcium* **2012**, *52*, 277–282. https://doi.org/10.1016/j.ceca.2012.04.001.
129. Kralj-Iglič, V.; Heinrich, V.; Svetina, S.; Žekš, B. Free energy of closed membrane with anisotropic inclusions. *Euro Phys J B-Conde Matter Complex Syst* **1999**, *10*, 5–8.
130. Snead, W.T.; Hayden, C.C.; Gadok, A.K.; Zhao, C.; Lafer, E.M.; Rangamani, P.; Stachowiak, J.C. Membrane fission by protein crowding. *Proc Natl Acad Sci USA* **2017**, *114*, E3258–E3267. https://doi.org/10.1073/pnas.1616199114.
131. Glotzer, S.C.; Solomon, M.J. Anisotropy of building blocks and their assembly into complex structures. *Nat Mater* **2007**, *6*, 557–562. https://doi.org/10.1038/nmat1949.
132. Liu, I.B.; Sharifi-Mood, N.; Stebe, K.J. Capillary Assembly of Colloids: Interactions on Planar and Curved Interfaces. *Annu Rev Conden Ma P* **2018**, *9*, 283–305. https://doi.org/10.1146/annurev-conmatphys-031016-025514.
133. Singh, A.P.; Rey, A.D. Computer-Simulation of Dynamics and Morphology of Discotic Mesophases in Extensional Flows. *Liq Crys* **1995**, *18*, 219–230. https://doi.org/Doi10.1080/02678299508036617.
134. Popkov, V.; Schutz, G.M. Unusual shock wave in two-species driven systems with an umbilic point. *Phys Rev E Stat Nonlin Soft Matter Phys* **2012**, *86*, 031139. https://doi.org/10.1103/PhysRevE.86.031139.
135. Liu, I.B.; Sharifi-Mood, N.; Stebe, K.J. Curvature-driven assembly in soft matter. *Philos Trans A Math Phys Eng Sci* **2016**, *374*. https://doi.org/10.1098/rsta.2015.0133.
136. Yao, L.; Sharifi-Mood, N.; Liu, I.B.; Stebe, K.J. Capillary migration of microdisks on curved interfaces. *J Colloid Interface Sci* **2015**, *449*, 436–442. https://doi.org/10.1016/j.jcis.2014.12.070.